

Treatment of early age-related macular degeneration in a cell culture model with femtosecond laser pulses

by

Katherine Nicole Smith

A thesis submitted in partial fulfillment of the requirements for the degree of

Master of Science

in

Photonics and Plasmas

Department of Electrical and Computer Engineering
University of Alberta

© Katherine Nicole Smith, 2017

Abstract

This thesis work focuses on obtaining preliminary results demonstrating the isolated femtosecond laser ablation of sub-RPE drusen-like deposits. Age-related macular degeneration (AMD) is an age-onset degenerative condition of the retina that can lead to legal blindness. The early stages of the condition are characterized by the development of hemi-spherical cellular debris accumulations, known as drusen, under the retina.

This project has two specific aims: demonstrating the laser ablation of AMD related sub-RPE deposits and assembling a prototype for a clinical therapeutic beam delivery system. An articulating arm is fitted with silver mirrors for 800 nm and coupled to a slit lamp ophthalmic device for femtosecond laser delivery to the retina.

A novel cell culture model using the immortalized cell line ARPE-19 is developed. The cell culture model is evaluated by confocal and transmission electron microscopy for the presence of sub-RPE drusen-like deposits. The samples are stained for two known drusen components, apolipoprotein E and cholesterol, to verify the artificial drusen-like deposits share a similar biochemical composition to drusen *in vivo*. Sub-RPE drusen-like deposits in the ARPE-19 model were targeted with 10 femtosecond pulse trains, 1.9-4.2 nJ/pulse, centered at 800 nm wavelength, from a Ti:Sapphire laser. Fluorescence microscopy was used to qualitatively confirm successful deposit ablation. After laser ablation more fluorescent dye was added to the dish and monitored to see if the areas targeted by the laser regain

fluorescence. Although areas of the sample did regain fluorescence, the targeted deposit accumulation never regained fluorescence. Thus, eliminating the possibility of laser photobleaching being responsible for deposit removal as opposed to plasma mediated breakdown.

To the friends and family who walked this journey with me,

I thank you with all my heart.

Acknowledgments

There are numerous individuals without whom this thesis work would not have been possible. Most prominently, I must acknowledge the efforts of my supervisor Prof. Abdulhakem Y. Elezzabi. His patience and guidance made this project what it was. I have learned so many lessons during my time under his tutelage that I will carry with me for the rest of my life. I am also very thankful for the financial support Dr. Elezzabi provided during my research.

I would like to thank my colleagues at the Ultrafast Optics and Nanophotonics Laboratory, Shawn Greig, Brett Carnio, Taylor Robertson, Curtis Firby, and Nir Katchinskiy, for their companionship. Your friendship and assistance along the way made this program very memorable. Special thanks to Shawn Greig for all of your assistance in working with the laser and to Nir Katchinskiy for your advice in the assembly of the slit lamp system.

I would like to thank all the others who made this research possible through offering their financial support and technical assistance. Dr. Ian MacDonald was an invaluable partner during this project. He significantly impacted the success of this research in his willingness to share his expertise and network of collaborators. I am very grateful for the expenses Dr. MacDonald was willing to incur during the course of this research. Special thanks go to Alina Radziwon for her expertise and tenacity during the development of the cell culture model. Her assistance and many work hours made this research possible. I thank Dr. Matthew Tennant for sharing his

knowledge and expertise throughout this project. Additional thanks go to Woo Jung Cho for his assistance in capturing TEM images of the cell culture samples.

All of my friends and family who supported me throughout this program have my sincerest thanks and endless gratitude. I surely would not have been able to do it without you. Kyle and Raven your generosity of love, encouragement, support, and nourishment was paramount to my ability to succeed and avoid malnutrition. In particular, I would like to thank my parents for their endless love and support, Isabelle Poon for knowing just when I needed someone to pick me up, and Brooklynn Knowles for the many cups of coffee and therapeutic conversations.

A special thanks to the Queen Elizabeth II Graduate Scholarship program for the financial support I received during my program, for which I am exceptionally grateful.

Table of Contents

Chapter 1 Introduction	1
1.1 Motivation	1
1.2 Age-Related Macular Degeneration	2
1.3 Ultrafast Optics	19
1.4 Thesis Scope	24
Chapter 2 Femtosecond laser pulse coupling to a slit-lamp	28
2.1 Introduction	28
2.2 Equipment	29
2.2.1 Slit lamp	30
2.2.2 Articulating arm	30
2.2.3 System integration	33
2.2.4 Future work	35
Chapter 3 Engineered model of dry AMD that develops drusen-like sub-RPE deposits	38
3.1 Motivation	38
3.1.1 AMD animal models	39
3.1.2 Primary cells vs. cell lines	39
3.1.3 Purpose of this study	41
3.1.4 Preliminary model attempts	42
3.2 ARPE-19 cell culture model	44

3.2.1 Experimental Methodology	44
3.2.1.1 Cell Culture	44
3.2.1.2 Confocal Microscopy	44
3.2.1.3 Electron Microscopy	46
3.2.2 Results	46
3.2.3 Discussion	58
Chapter 4 Isolated femtosecond laser pulse ablation of sub-RPE drusen-like deposits	63
4.1 Motivation	63
4.1.1 Laser treatments for AMD	65
4.1.2 Purpose of this study	65
4.2 Femtosecond laser pulse ablation of sub-RPE deposits	67
4.2.1 Experimental Methodology	67
4.2.1.1 Fluorescence imaging and laser delivery setup	67
4.2.2 Results	68
4.2.3 Discussion	76
Chapter 5 Conclusion and future prospects	82
5.1 Conclusion and future prospects	82
5.1.1 Histological and viability assay	83
5.1.2 Future prospects	85
References	87
Appendix A	100
Appendix B	104

List of Figures

Fig. 1.1: Cross-sectional view of the multi-layered structure known as the retina. The inner limiting membrane is the inner most layer of the retina, closest to the anterior section of the eye. The pigment epithelium monolayer is the outer most layer of the retina, closest to the choroid and back of the eye. Bruch’s membrane lies next to the retinal pigment epithelium. Adapted from [9]. 3

Fig. 1.2: Horizontal cross-section of the eye, giving a top down view. Many important structures of note are labeled, in particular the macula lutea and the choroid. Adapted from [11]. 4

Fig. 1.3: Fundus image of the retina of an individual with early AMD. Several drusen over 125 μm in diameter are visible as the diffuse, yellowish shapes. The fovea, which lies at the center of the macula, is indicated by the asterix. Adapted from [29]. 9

Fig. 1.4: Cross sectional view of the multi-layered retina with multiple drusen visible. The innermost layers of the retina are at the bottom of the image while the choroidal blood vessels are the top most layer visible. Drusen, labeled with an asterix, are growing between the RPE and Bruch’s membrane. Adapted from [29]. 10

Fig. 1.5: Transmission electron microscopy images of a retina with and without drusen formation. The top image shows a normal, healthy eye with the RPE monolayer and Bruch’s membrane (BM) undisturbed. The bottom image shows the

mechanical disruptive result of drusen (D) formation. The RPE monolayer is significantly displaced, and as a result the RPE cells are seriously disfigured. The arrowheads point to RPE cell. Adapted from [29]. 11

Fig. 1.6: Fundus image of the retina of an individual with early age-related macular degeneration. The white circle highlights an area of hard drusen formation under the retina. The drusen spots appear as very small yellowish pinpoints against the red/orange retina. At the hard drusen stage the accumulations are typically less than 60 μm and have well defined borders. (Arrow: pigment disruption). Adapted from [29]. 13

Fig. 1.7: Fundus image of the retina of an individual with soft drusen (white oval). The accumulations are not uniformly shaped, have very irregular borders, and ill-defined edges. Many of the bright yellow accumulations are visibly larger than 60 μm . Adapted from [29]. 14

Fig. 1.8: Depiction of proposed femtosecond laser assisted treatment for AMD. The only laser-tissue interaction will occur at the focal point of the laser beam, which can be precisely applied to the sub-RPE drusen. The drusen are laser ablated without collateral damage to any of the important surrounding tissue. 25

Fig. 2.1: The completed power circuit for the slit lamp. A refurbished computer fan maintains an adequate operating temperature for the heat sink laden resistors. 31

Fig. 2.2: Redesigned safety circuit for the beam-blocking shutter housed in the binocular chamber of the slit lamp device. 32

Fig. 2.3: Custom designed and machined anchor for the horizontal section of the articulating arm. The Aperture is mounted on the front of the arm opening to aid in

alignment procedures. The right image shows a diode laser beam entering the articulating arm pathway after successful alignment. 34

Fig. 2.4: Fully assembled prototype of femtosecond retinal surgery device. The images show the articulating arm connected into the slit lamp mirror mechanism. The condensing lens is housed in the silver adapter between the black arm and black mirror mechanism. The diagnostic white light and red “treatment” beam can be seen on the blue target mounted on the dummy. 36

Fig. 3.1: Confocal microscopy images with ApoE antibody staining of the two different culture samples. (A) Shows the experimental sample of ARPE-19 cells grown for five-weeks. (B) Shows the control sample of cells grown only until confluence. The control sample in (B) shows no deposit immunoreactivity compared to (A.) (Scale bars, 50 μm in A and B.) 48

Fig. 3.2: Confocal microscopy image of 5-Week and 3-Day ARPE-19 cell culture samples and the filtered image after using a mask to isolate deposit accumulations. (A) and (C) are the original confocal image of a 5-Week and 3-Day sample, respectively. (B) and (D) are the images obtained after applying a mask created in MATLAB to isolate pixels of deposit accumulations. The pixel threshold mask values quantitatively demonstrated the experimental sample in A/B shows more deposit accumulation than the control sample in C/D. 49

Fig. 3.3: Confocal microscopy image of a 5-Week ARPE-19 sample treated with filipin. The circles indicate a number of cholesterol rich sub-RPE deposits stained intensely with filipin. (Scale bar, 500 μm .) 50

Fig. 3.4: Confocal microscopy image of a 5-Week ARPE-19 sample stained simultaneously with ApoE and filipin. The circle in each image outlines the same sub-RPE deposit in each channel. (A) Shows both the ApoE and filipin channels overlaid indicating the co-localization of ApoE and cholesterol in the deposit. For clarity, the individual stain channels are separated to further emphasize the co-localization with ApoE in (B) and filipin in (C). (Scale bars, 25 μm in A, B, and C.) 52

Fig. 3.5: TEM images of sub-RPE deposits formed in a 5-Week ARPE-19 cell culture. (A) An area of condensed deposit formation (*circle*). (B) Examples of membranous deposits (*ellipse*). (C) Shows an area of fibrillar deposit formation (*ellipse*) as well as highlighting a membranous deposit also visible in this area (*arrow*). The cell layer and porous membrane are labeled in each image. (Scale bars, 500 nm in A, B, and C.) 53

Fig. 3.6: TEM image shows the distance, as labeled, between the ARPE-19 cell layer and the porous membrane when (A) deposits are present (*ellipses*: Condensed deposits) and when (B) no deposits are formed. The cell layer and porous membrane layer are labeled in each image. 55

Fig. 3.7: TEM images showing examples of cellular debris deposits lodged in the channels of the 0.4 μm pores of the porous membrane. (A) Shows a single pore with three membranous deposits lodged in the pore. (B) Shows two pores in the membrane with a membranous deposit in one of the pores. The insert in each image provides a zoomed-in view of the deposits for improved contrast. The PET

membrane, cell layer, and pore openings are labeled in each image. (Scale bars, 500 nm in *A* and *B*.) 56

Fig. 3.8: Confocal microscopy image with ApoE staining of an ARPE-19 cell culture after the five-week incubation period and the cell layer has been removed using trypsin. The circle indicates the presence of a sub-RPE deposit on the porous membrane, even after the removal of the cell layer. (Scale bar, 50 μm .) 57

Fig. 4.1: Representation of the laser pulse-tissue interaction between the femtosecond laser pulses and sub-RPE drusen-like deposits. The femtosecond pulse trains pass harmlessly through the ARPE. The threshold leading to plasma-induced ablation is only surpassed at the point of focus of the laser, herein located on the drusen-like accumulation. 69

Fig. 4.2: Image captured through a microscope at 60x of an ARPE19 cell in the various categorical stages of interaction with the laser pulses during investigation into ablation parameters. (*A*) shows the cell upon initial inspection, prior to any laser pulse exposure. In (*B*), the first visual evidence of femtosecond pulse interaction with the cell is visible. A large, lasting cavitation bubble induced by pulse exposure windows is seen in (*C*). In (*D*), the cell has been significantly deformed and areas a fluid leakage from the cell are highlighted by a red outline. The cell outline is highlighted by a black dotted line in each image 71

Fig. 4.3: Fluorescence microscopy image, stained for ApoE, of a sub-RPE deposit before and after unsuccessful laser ablation. The plane of focus was on the ARPE-19 cell layer in (*A*) and (*B*) and was below the cells on a sub-RPE deposit in (*C*) and

(D). (A) and (C) were taken before the laser pulse exposure and (B) and (D) were taken after the laser delivery. (A) shows the fluorescent signal of the deposit visible through the cell layer. (B) highlights the shadow of scarring caused by damage to the cell layer during laser delivery to the sub-cellular space. (C) shows the deposit before laser ablation. (D) demonstrates the absence of the deposit after laser pulse delivery. The white circle highlights the same area of interest in each image. (Scale bars, 10 μm in A-D.) 72

Fig. 4.4: Fluorescence microscopy, using ApoE staining, before and after the successful laser ablation of a sub-RPE drusen-like deposit. The focal plane was on the ARPE-19 cell layer in (A) and (B) and was below the cells on a sub-RPE deposit in (C) and (D). (A) and (C) were taken before the laser pulse exposure and (B) and (D) were taken after the laser delivery. In (A), the fluorescence of the sub-cellular deposit, shown in (C), can be seen through the cell layer. In both (B) and (D), the deposit is no longer visible and there is no damage or scarring to the cell layer as shown in (B). The white circle in each image highlights the same area of interest. (Scale bars, 20 μm in A-D.) 74

Fig. 4.5: Fluorescence microscopy image of a sub-RPE deposit, stained simultaneously for ApoE and cholesterol, before and after laser ablation. The ApoE channel is shown before (A) and after (B) laser ablation. The filipin channel is shown before (C) and after (D) laser ablation. The two inserts in each image show the normalized plots of pixel intensities along the vertical (top right) and horizontal (bottom right) lines seen in each frame. Before laser ablation, in (A) and (C), the line intensity plot shows the profile of the sub-RPE deposit. After laser ablation, the

deposit contour has been destroyed, see (B) and (D). More filipin stain was added after (D) was taken. (E) is after 80 minutes had passed, areas within the image begin to regain fluorescence, but the deposit area pixel intensity does not return. The white circle in each image highlights the same region of interest. The white arrowheads in (C)-(E) label a fluorescent deposit used as a landmark during the image acquisition. (Scale bars, 20 μm in A-E.) 75

Fig. 4.6: Filipin fluorescence microscopy of an ARPE-19 sample with sub-RPE deposits. (A) was taken immediately after the excitation shutter was opened, showing the baseline fluorescence for the sample. (B) shows the photobleached sample after prolonged and continual excitation source exposure. More filipin stain was added to the dish after (B) was taken. (C) was taken 60 minutes after the addition of more filipin and shows that some cholesterol rich deposits regain their fluorescence after photobleaching if more filipin is added. (Scale bars, 20 μm in A-C.) 77

Fig. A.1: OCT image of retina layers. (A) and (B) show two images of the same retina. In (C) and (D) the vertical depths of many identifiable and important retinal membrane layers are plotted along the white lines as seen in (A) and (B). Adapted from [101]. 101

Fig. A.2: Graphical representation of the retina. Many important cell layers and boundary membranes between different cell types are labeled. Adapted from [9]. 102

Fig. A.3: Histological cross-section of a human retina. The various cell layers are labeled on the left with the bounding membranes and layers on the right. Outer

limiting membrane (OLM). Outer nuclear layer (ONL). Outer plexiform layer (OPL). Inner nuclear layer (INL). Inner plexiform layers (IPL). Ganglion cell layers (GCL). Inner limiting membrane (ILM). Adapted from [9]. 103

List of Symbols and Abbreviations

A2-E	<i>N</i> -retinylidene- <i>N</i> -retinylethanolamine
AMD	Age related macular degeneration
Anti-VEGF	Anti-vascular endothelial growth factor
ApoE	Apolipoprotein E
AREDS	Age related eye disease study
AREDS2	Age related eye disease study 2
ARPE	Artificial retinal pigment epithelium
BrM	Bruch's membrane
BRB	Blood retina barrier
BSA	Bovine serum albumin
ER	Endoplasmic reticulum
Fs	Femtosecond
LASIK	Laser-assisted in situ keratomileusis
LED	Light emitting diode
OCT	Optical coherence tomography
OS	(Photoreceptor) Outer segments
PBS	Phosphate-buffered saline
PBST	Phosphate-buffered saline + 0.1% Tween 20
PET	Polyethylene terephthalate
RPE	Retinal pigment epithelium

TEM Transmission electron microscopy

Chapter 1

Introduction

1.1 Motivation

Femtosecond pulse lasers have a variety of applications, but in recent years the field of particular interest has been the interaction of femtosecond laser pulses with biological tissues. The duration of a femtosecond is one millionth of a billionth of a second. On this time scale, the absorption process of laser pulses by tissue is unique from the behavior of other, longer pulse durations. In interacting with biological tissue and cells, high power femtosecond laser pulses can be absorbed by such material via nonlinear multiphoton absorption. This process can distinctively alter sub-cellular structures within a near diffraction limited spot size [1–4]. The pulse duration of femtosecond lasers is below the threshold for many destructive laser pulse-tissue interaction events, such as heat dissipation, cavitation bubble formation, and shockwave generation.

The distinctive laser pulse-tissue interaction qualities of femtosecond pulse lasers make them an excellent tool in the biomedical field. These optical systems possess particularly important potential as therapeutic medical devices. This thesis focuses on femtosecond laser pulses' capacity to be a clinical tool for the treatment

of age-related macular degeneration (AMD). This chapter presents a background overview of the condition age-related macular degeneration and the current knowledge on the laser-tissue behavior of femtosecond lasers.

1.2 Age-Related Macular Degeneration

Age-related macular degeneration is an age-onset degenerative condition affecting the focused, central field of vision. AMD is the leading cause of blindness in the developed world [5–7]. The chances of developing AMD are 1 in 10 for people over the age of 65 and 1 in 4 for those over the age of 75. This disease costs health care systems millions of dollars a year and affects more people than breast cancer, prostate cancer, Alzheimer’s disease, and Parkinson’s disease combined [8]. To investigate age-related macular degeneration, it is important to have an understanding the key parts of ocular physiology affected by and involved in the development of this disease. The retina is a multi-layered structure comprised of several different cell types: nerve cells, epithelium, photoreceptors, etc. (Fig 1.1) (A breakdown of the dimensions of the layers of the retina can be found in Appendix A) [9, 10]. The oval-like region near the center of the retina, which is exceptionally densely populated with cone photoreceptors, is known as the macula. The macula, as indicated in Fig. 1.2, represents merely 4% of the total retinal area and is responsible for sharp central visual acuity while the rest of the retina provides peripheral vision [9, 11]. It is in this important region densely populated by cone photoreceptors where AMD develops. The outer most layer of the retina is the retinal pigment

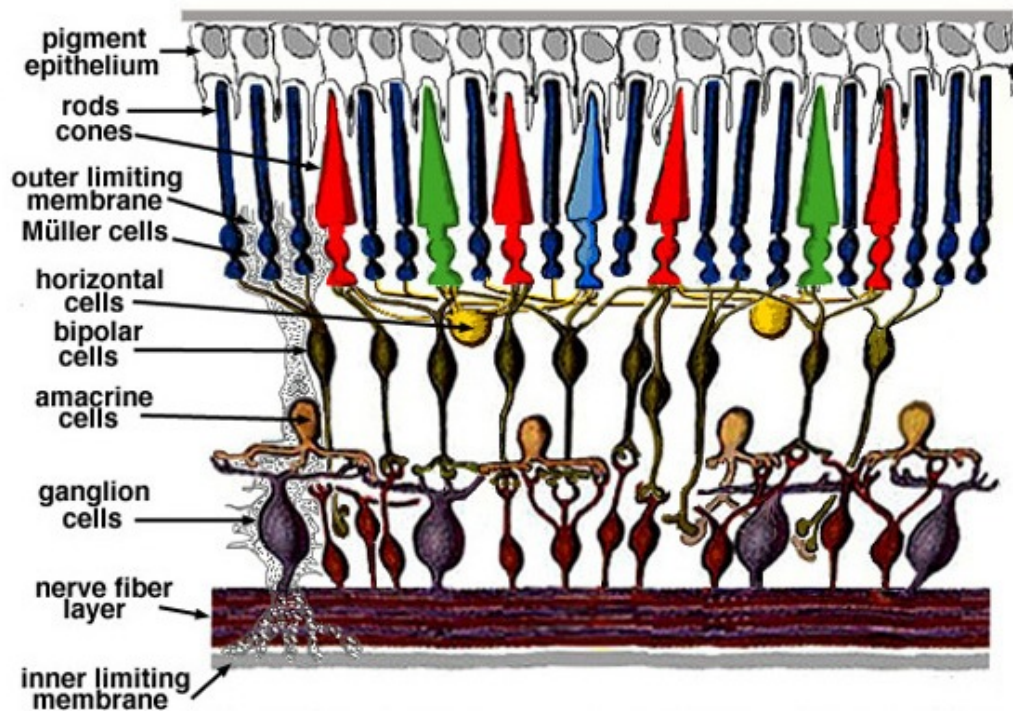


Fig. 1.1: Cross-sectional view of the multi-layered structure known as the retina. The inner limiting membrane is the inner most layer of the retina, closest to the anterior section of the eye. The pigment epithelium monolayer is the outer most layer of the retina, closest to the choroid and back of the eye. Bruch's membrane lies next to the retinal pigment epithelium. Adapted from [9].

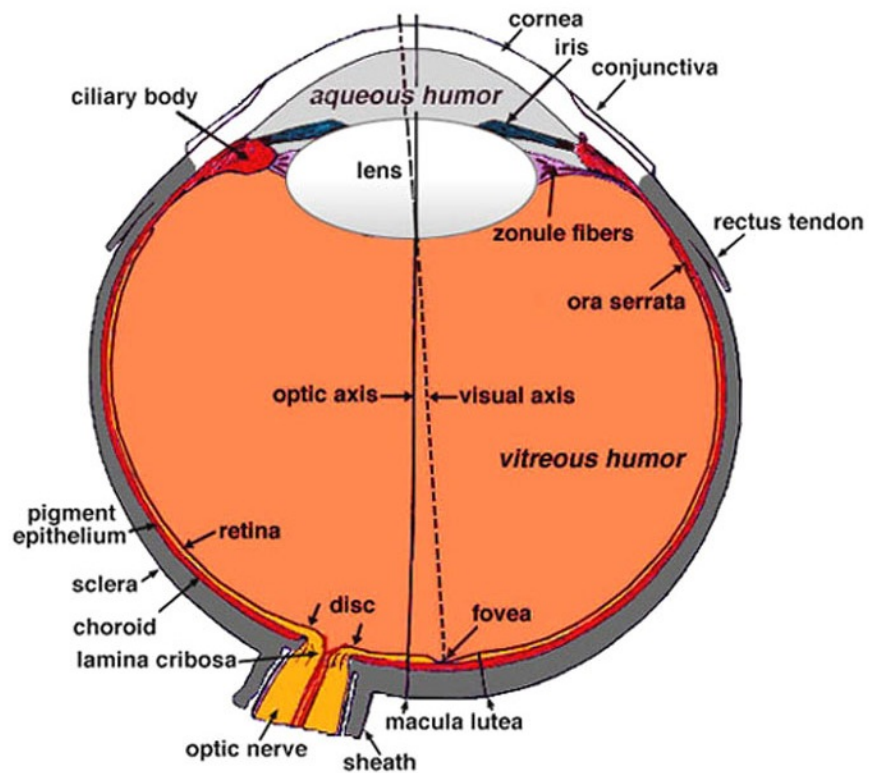


Fig. 1.2: Horizontal cross-section of the eye, giving a top down view. Many important structures of note are labeled, in particular the macula lutea and the choroid. Adapted from [11].

epithelium (RPE), a monolayer structure of hexagonal epithelial cells, as seen in Fig. 1.1, that average 10-14 μm thick [12]. The RPE cells execute a variety of tasks critical to the healthy operation and survival of photoreceptors. This includes the phagocytosis of shed photoreceptor segments to recycle and restore nutrients back into the cells as well as the secretion of a variety of very important growth factors including vascular endothelial growth factor [13–15]. Cellular debris not adequate for recycling back in towards the photoreceptors is shed basally and cleared away by the choroidal blood vessels. Behind the RPE layer, just outside the retina, is the choroid, a multi-layer connective tissue body that is a major part of the vascular system for the retina (Fig 1.2) [9, 16]. Blood vessels in the choroid bring nutrients and oxygen to the outer layers of the retina, particularly the photoreceptors and RPE. The RPE performs many of the same functions for the eye as the blood-brain barrier does for the brain [17]. The oxygen tension in the choroidal blood vessels (i.e. choriocapillaris) must be significant enough to satisfy the very high oxygen demand of the outer retina and the flow of oxygen from the choroid into the retina. Consequently, the choroid blood flow exceeds that of even the brain by a margin of ten times, assumed to be the highest blood flow per unit tissue-weight within the body [16]. Though the central retinal artery also provides oxygen to the retina, specifically the innermost cell layers, the choroid supplies at times up to 90% of the oxygen requirement of the retina. The inner most layer of the choroid is a 2-4 μm thick layer called the Bruch's membrane (BrM) [9, 18]. On top of symptoms affecting the retina, changes to the BrM are also observed in patients with AMD, in particular the thickening and reduced permeability of the BrM [10]. Debris

accumulations are also observed within the aging BrM, compounding the permeability issues. The flow of oxygen and nutrients from the choroid into the retina, and of cellular debris from the retina into the choroid is critical to healthy cell function in the retina. Therefore, substantial and sustained alterations to the composition or thickness of the BrM can be very destructive for the RPE, and more importantly the photoreceptors of the retina. The reactive oxidative compounds produced during the cellular metabolic process can become trapped within the outer layers of the retina due to the lack of vasculature in the area. As people age, and the cells degrade, no longer functioning at full efficiency, it becomes more difficult for them to process and remove the reactive oxidative species [19–22]. Thus, the toxic concentration in the area increases. Many researchers believe this oxidative stress to be a significant contributor to AMD progression.

There is a threshold for “acceptable” age related changes to the eye; over a lifetime of constant light excitation photoreceptors become less efficient and the RPE no longer recycle the shed outer segments of photoreceptors effectively [10]. RPE cells are classified as post-mitotic, meaning that they do not regenerate under normal circumstances, although have previously been artificially stimulated *in vitro* to undergo proliferation [23, 24]. With age, the rate at which these cells are lost increases, which in turn increases the photoreceptor metabolism load per cell and stresses the remaining cells. Many researchers have identified increasing levels of the round, yellow, autofluorescent granular accumulation called lipofuscin in “normal” aging RPE [10, 13, 25, 26]. Approximately 8% of the RPE cytoplasmic space is filled by lipofuscin for patients at 40 years of age, increasing to 90% when

they reach the age of 80 [10]. Lipofuscin is thought to be a byproduct of the phagocytosis of photoreceptor outer segments by RPE cells. As reported by Katz and Robison [26], if the degradation and recycling process of outer segments is interrupted the remaining photoreceptor material within the RPE cell quickly becomes lipofuscin-like materials. Investigations into the effects of lipofuscin, and its primary fluorophore *N*-retinylidene-*N*-retinylethanolamine (A2-E), have shown it to be toxic and detrimental to cell function though the precise mechanism by which the lipofuscin induces cell dysfunction varies between different scientific reports [10, 19, 27]. Increasing lipofuscin levels have a direct relationship to significant photoreceptor loss in aging eyes [25]. Several investigators have suggested various theories about lipofuscin induced cell dysfunction including impeded cell function due to reduction in cytoplasmic space. Alternatively, it has been shown that A2-E interrupts the RPE phagocytotic process through inhibiting normal lysosomal process as it raises pH levels [10, 19, 27]. Outside of the functional pH range, the efficiency of the lysosomal enzymatic activity is significantly reduced and cannot fully perform the photoreceptor breakdown. The altered lysosomes may start to leak enzymes into the cytoplasm, irreversibly damaging the cell membrane and inducing cell death by apoptosis. Experimentally, many investigations have shown AMD like symptoms to develop after three types of manipulation: antioxidant deficiency, oxidization of photoreceptor outer segments, and inhibition of lysosomes [19]. Though there is a clinically acceptable threshold of RPE cell death and lipofuscin accumulation in elderly patients, the rates of both of these processes are significantly

increased with the onset of AMD and can be a strong indicator of imminent progression to more severe symptoms.

The exact pathology of AMD remains unknown, as it is a complicated combination of several polygenic and epigenetic factors [28, 29]. A variety of different genes, at several different chromosomal loci have been identified as contributors to the inheritance and development of AMD [20]. Additionally, several environmental risk factors, such as obesity and smoking, are known to significantly increase the chances of developing or aggravating AMD symptoms [29, 30]. Age-related macular degeneration is categorized into two pathological stages, early and late, each with different symptoms and degrees of severity [10, 29]. The earliest stages of AMD are characterized by the accumulation of organic material into toxic deposits, known as drusen, between the RPE and the first layer of Bruch's membrane [10, 29, 31–34]. Drusen are yellowish accumulations that are easily identifiable through visual inspection by trained medical professionals or on fundus images, as seen in Fig. 1.3. Drusen are hemispherical accumulations of lipids and proteins and are considered clinically significant after reaching a diameter of 63 μm [10, 29]. The development of drusen between the outer retina and the choroid displaces the RPE, creating significant mechanical stress on the individual cells and the monolayer structure as a whole, as seen in Fig. 1.4 and 1.5 [35]. As a result of the mechanical stress, RPE cells begin to die and leave holes in the monolayer. A snowball effect is created as this in turn produces even more stress, as remaining RPE cells must physically shift to try to fill in holes and must work harder to recycle photoreceptor segment to compensate for reduced RPE cell numbers. Two distinct



Fig. 1.3: Fundus image of the retina of an individual with early AMD. Several drusen over 125 μm in diameter are visible as the diffuse, yellowish shapes. The fovea, which lies at the center of the macula, is indicated by the asterisk. Adapted from [29].

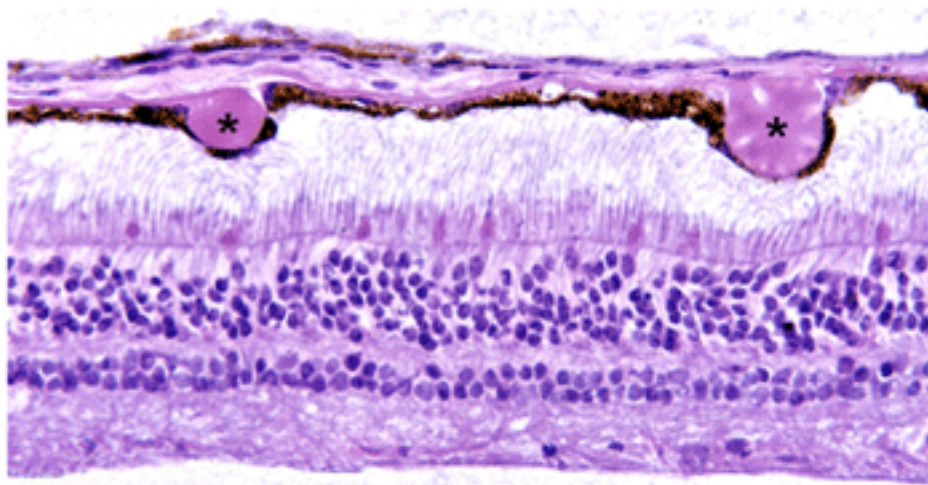


Fig. 1.4: Cross sectional view of the multi-layered retina with multiple drusen visible. The innermost layers of the retina are at the bottom of the image while the choroidal blood vessels are the top most layer visible. Drusen, labeled with an asterix, are growing between the RPE and Bruch's membrane. Adapted from [29].

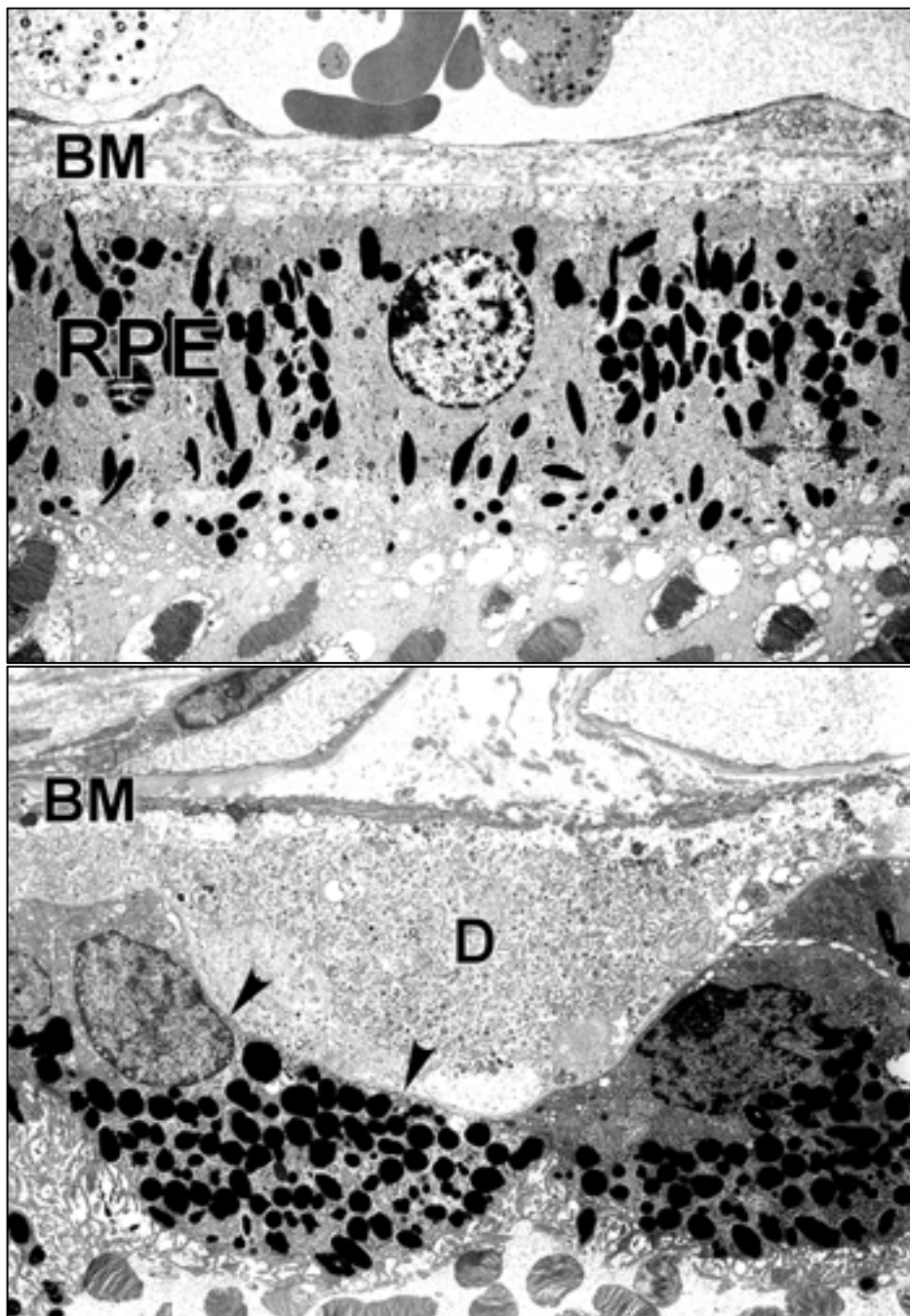


Fig. 1.5: Transmission electron microscopy images of a retina with and without drusen formation. The top image shows a normal, healthy eye with the RPE monolayer and Bruch's membrane (BM) undisturbed. The bottom image shows the mechanical disruptive result of drusen (D) formation. The RPE monolayer is significantly displaced, and as a result the RPE cells are seriously disfigured. The arrowheads point to RPE cell. Adapted from [29].

varieties of drusen are identifiable on the retina and are known as hard or soft drusen. Hard drusen, seen in Fig. 1.6, are small, yellowish formations typically up to 60 μm in diameter that protrude upwards, displacing the RPE monolayer, on the order of 30 μm [35, 36]. They are the first type of drusen observed in an aging retina, and having a small number of them present during examination of the retina is considered part of the normal aging process. These types of drusen have well-defined edges that are easily identifiable during imaging of the retina. Hard drusen can enlarge and become soft drusen, which have a paler colour, ill-defined edges, and large diameter (Fig 1.7). The appearance of soft drusen on the retina is considered a serious risk factor for progression to later, more serious stages of AMD. A large number of studies have been done that investigate the biological composition of drusen. A variety of lipids and over 120 distinct proteins were identified in drusen isolated from several different donors [34, 36–38]. It is quite possible that the cytokine secretions RPE use to communicate with surrounding cells are also present in drusen [13, 15]. Of particular note, is the possibility that the RPE secreted vascular endothelial growth factor is present in drusen. Prolonged accumulation of the endothelial growth factor between the RPE and BrM could be a catalyst for the neovascular growth in later stages of AMD. The most common lipid found during composition studies was cholesterol, and although both esterified and unesterified cholesterol were found, esterified cholesterol was by far the most prominent neutral lipid. Wang et al. [36] found that in sampled drusen, the combined weight of lipids surpassed the combined weight of proteins 3-fold. Identifying the major components of drusen was an important step in future

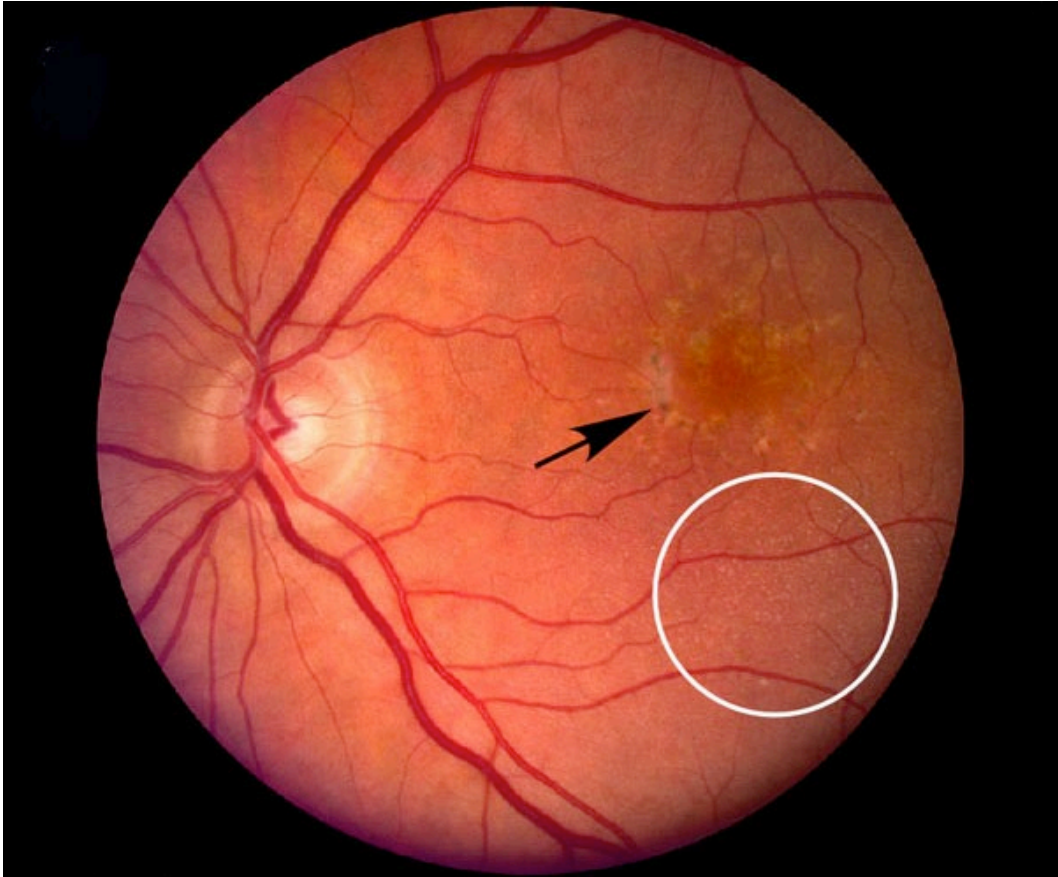


Fig. 1.6: Fundus image of the retina of an individual with early age-related macular degeneration. The white circle highlights an area of hard drusen formation under the retina. The drusen spots appear as very small yellowish pinpoints against the red/orange retina. At the hard drusen stage the accumulations are typically less than 60 μm and have well defined borders. (Arrow: pigment disruption). Adapted from [29].

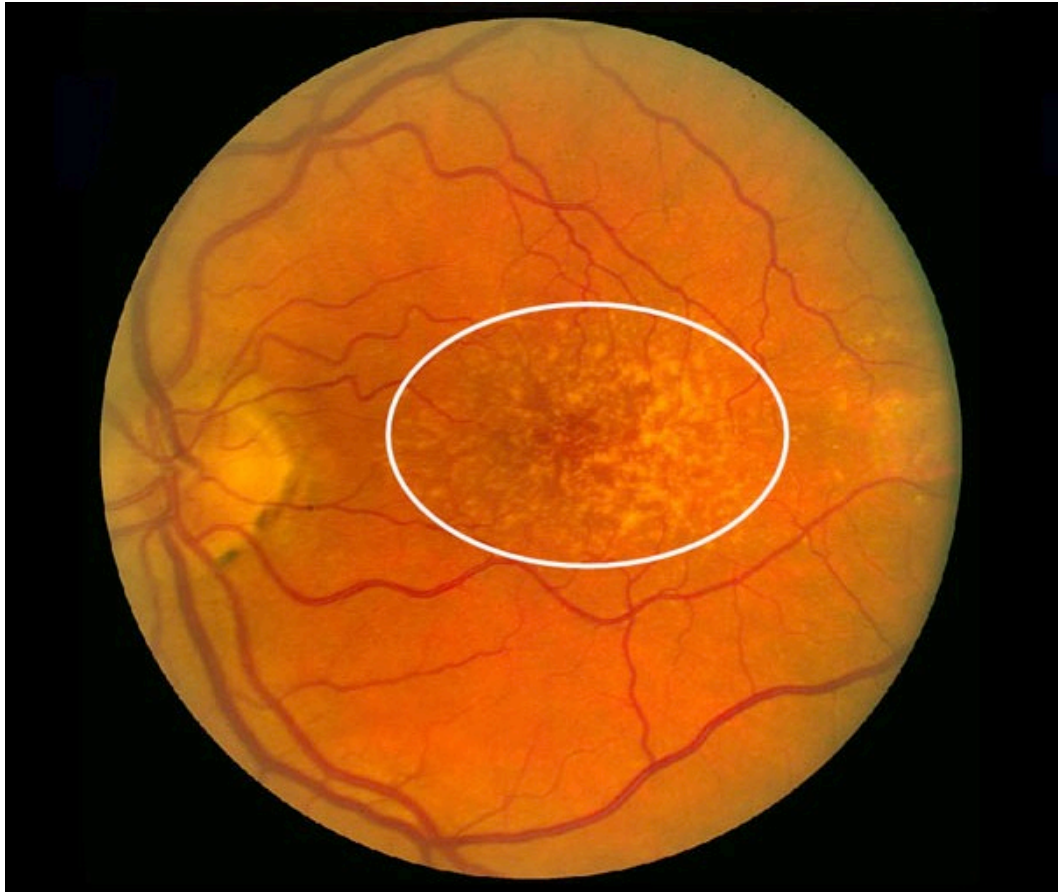


Fig. 1.7: Fundus image of the retina of an individual with soft drusen (white oval). The accumulations are not uniformly shaped, have very irregular borders, and ill-defined edges. Many of the bright yellow accumulations are visibly larger than 60 μm . Adapted from [29].

investigators being able to appropriately model this condition for study. Drusen are the distinguishing features that herald AMD, understanding their structure and the effects they exert on the cellular environment is critical to furthering knowledge of AMD and exploring ways to treat the condition.

Early AMD severity is graded on a scale, developed by the Age-Related Eye Disease Study (AREDS) clinical trial, from stages 1 to 9 based on the size, shape, and number of drusen identified on fundus images of patients' retinas [39, 40]. At stage 9, a case is considered late stage AMD and two distinct types of late stage AMD exist based on the form of degeneration present in the retina. Late stage dry AMD is known as geographic atrophy, it presents as large areas of pigment loss due to RPE and photoreceptor death [10, 29]. The second category of late stage AMD is often referred to as wet or neovascular AMD. It is characterized by the development of choroidal neovascularization into the retina as blood vessels from the choroid grow through breaks in the BrM and begin to exude fluid and blood components into the retina. The symptoms of wet AMD are significantly more severe than those of dry AMD, with neovascularization causing at least 80% of legal blindness associated with the disease [10]. Almost all cases of choroidal neovascularization result from the progression of already identified clinical cases of early AMD, with wet AMD hardly ever developing spontaneously. While wet AMD is more detrimental when compared to dry AMD, only 10-15% of cases progress to the advanced wet form [10, 29]. Yet, the majority of contemporary treatment methods have focused exclusively on late stages of the disease.

Currently, there is no cure for AMD. Preventative strategies that manage symptoms in the latest stages of the disease and attempts to slow progression from early to late stage exist. However, no method of completely halting the progression or reversing vision loss that has already occurred has been found. The Age-Related Eye Disease Study (AREDS), a two stage multi-center clinical trial, investigated the risk factors and progression of AMD as well as the effectiveness of treatment with a proprietary combination of vitamins called the AREDS formula [40, 41]. The first stage of the trial (AREDS) ran from 1999-2001 and after some minor adjustments to the supplement recipe, the trial ran in a second stage (AREDS2) from 2006-2012. Participants in the study that did not receive a placebo injection were dosed with a concentrated formulation of antioxidants. The AREDS formula only produced a statistically significant reduction in progression rates in groups already suffering from intermediate AMD in both eyes or advanced AMD in one eye [41]. The advantage from the antioxidant formula only amounted to a 25% reduction in the risk of developing advanced AMD over a 5-year follow up window. There was no significant advantage bestowed on individuals in the earliest stages of AMD, which equates to 80% of people with AMD over the age of 70. All other current and discontinued treatment strategies target very advanced AMD [42]. On top of late stage AMD only encompassing around 10% of cases of the disease, it is a progressively degenerative condition. Therefore, halting the condition in the earliest stages is paramount to minimizing the retinal damage and visual deterioration from the disease and maximizing the quality of life maintained by the patient.

Previous attempts at treatments for AMD, in addition to the AREDS formulation, include laser photocoagulation, photodynamic therapy, and anti-vascular endothelial growth factor (anti-VEGF) injections [10, 29, 43, 44]. As with the antioxidant supplements, these treatment strategies are not cures for AMD but strategies to manage the symptoms and delay progression of the disease, with varying degrees of success. Currently, intraocular anti-VEGF injections are the gold standard for treatment of wet, late stage AMD [17, 43, 45]. The inhibitors work to curb the growth of choroidal blood vessels into the retina, attempting to slow the damage caused by neovascularization. However, the treatment protocol requires regularly repeated intraocular injections of the vascular growth inhibitors, which can be uncomfortable for the patient. Additionally, a point of concern with this treatment method is the potential for the administered anti-VEGF to affect other structures in the body, as it is not a target selective substance [29]. It has been suggested that the anti-neovascular agents could also affect the heart or brain and even inhibit wound-healing capabilities. Though there are currently many investigations underway, the effects of prolonged exposure to the anti-VEGF drugs are currently unknown and could present a serious downside to this new treatment strategy.

Multiple attempts to harness the power of lasers to treat AMD have been made. The two laser treatment techniques attempted in a variety of forms are photocoagulation and photodynamic therapy [10, 29, 44, 46–53]. Most AMD photocoagulation treatment protocols involved the use of 805 nm diode lasers targeted at choroidal neovascular growth in the retina in an attempt to cauterize the leaky blood vessels. However, the laser application induced fulminant, untreatable

neovascularization recurrences and large, visible retinal scars. Additionally, the possibility of non-specific laser exposure inducing drusen resorption or photobleaching AMD fluorophores has been investigated. Manevitch et al. [54] tried to photobleach away all A2-E from individuals with drusen and other AMD symptoms. The drawback of this strategy is that A2-E is a component in lipofuscin, which is diffuse throughout the retina. Therefore, an attempt to treat AMD by bleaching A2-E requires the entire retina be the target area. Friberg et al. [49, 50] attempted to induce drusen resorption through laser photocoagulation using 810 nm continuous wave diode lasers. A fixed treatment grid pattern of 48 laser spots was delivered to the subjects' retinas. Although short-term drusen resorption was observed, long-term visual outcomes did not present any benefit in the laser treated group. In fact, several clinical trials investigating the treatment of AMD through laser induced drusen resorption were abandoned after the treatment was quickly shown to be increasing the rate of progression to wet AMD [49, 50, 55]. This could potentially be attributed to the continuous wave diode lasers used inflicting significant thermal and mechanical collateral damage to the retinal tissue surrounding the grid spots. The thermal energy deposition characteristic of these laser systems is important when the goal of the treatment is to cauterize, essentially welding the blood vessels shut. However, during patterned application to the retina to induce drusen resorption, it is very likely that the same thermal energy deposition lead to significant damage to retina cells. Most clinicians eventually abandoned laser photocoagulation as a treatment for AMD as the therapeutic benefits did not statistically significantly out-weigh the collateral damage done.

During photodynamic therapy a photosensitive substance, typically verteporfin, is injected systemically [47, 48, 56]. After a period of time to allow the substance to diffuse to the desired target location, the photosensitive material is excited via a laser beam. Endothelial cell death is induced from thermal energy generation in an attempt to cauterize the neovascular blood vessels [47]. This treatment method is also attributed with significant collateral damage because the photosensitive substance injected into the patient is not specific to the targeted tissue or region. During laser light activation of the photosensitizer, thermal energy can transfer to nearby healthy tissue both due to proximity to a targeted region with photosensitizer present as well as the substance being absorbed by the healthy tissue. Both previous attempts at laser-assisted treatment discussed herein have highly non-specific targeting protocols. The side effects of the treatment procedures from collateral damage to healthy tissue over-shadow the potential therapeutic benefits [46, 48]. It is important to acknowledge the shortcomings of previous laser-assisted treatments for AMD and to learn from and incorporate the lessons into future attempts at laser-based treatments for this debilitating condition.

1.3 Ultrafast Optics

Ultrafast optics is the division of optics studies on the picosecond to femtosecond time scale. The interaction between a femtosecond laser pulse and a biological material is fundamentally different than the interaction between that same material and a longer pulse duration or continuous wave laser. This has to do with

the electron relaxation time of the material [1, 57, 58]. The mechanism of interaction between a laser and incident material depends on a wide variety of parameters including: wavelength, intensity, exposure window, material composition, and absorption of the material [57]. A fundamental understanding of the laser pulse-tissue interaction of femtosecond laser pulses is required to apply this technology as a clinical tool.

The depth of penetration of light into a biological tissue is determined by a multitude of factors including the wavelength of a laser and the type of interaction, whether thermal, mechanical, or chemical, is determined by the pulse duration [1]. Lasers are a convenient and viable tool for treatment of retinal conditions due to the transparent nature of the cornea and lens of the eye. This transparency enables a treatment beam to be delivered to the retina without significant absorption or scattering along the path prior to the desired target on the retina. A therapeutic window has been quantified to exist for lasers of wavelengths between 600 – 1200 nm as the water and macromolecules that comprise the eye are nearly totally transparent to these wavelengths, and the laser beam can penetrate deeper than is possible in other tissues or materials [1]. With uniquely chosen laser parameters, including wavelength, as mentioned, but also pulse length and energy per pulse, the laser light will travel through the anterior structures of the eye, only interacting with and producing laser ablation at the focal point of the beam. In what is known as non-linear, multiphoton absorption, the beam will traverse the material above the area of interest harmlessly and will not continue below the desired plane, limiting collateral damage.

As mentioned previously, the type of interaction between the laser pulse and the tissue varies based on a multitude of beam specific variables. The different interactions include thermal coagulation, photochemical effects, vaporization, and plasma formation [1, 57]. A laser becomes a heat source if the thermal relaxation rate of the target material is shorter than the pulse duration of the incident pulse [1, 59]. Therefore, an ultrashort pulse duration can interact with materials prior to the thermal relaxation time and thus not deposit thermal energy to be diffused throughout the target. This is critically important in biological tissues as catastrophic and irreversible damage can occur within a small window of temperature rise. When the biological tissue temperature reaches 42°C, there are few noticeable changes to cellular tissues; however, cellular membrane breakdown occurs between 42-50°C, proteins and other cellular materials are denatured above 60°C, and water boils and is vaporized at 100°C. Major damage is done to biological material within an 18°C range [1]. Thus, when the intended goal involves laser interaction with biological tissue, minimizing heat deposition in the tissue is critical to the preservation of healthy tissue and that is why femtosecond laser pulses are so important for such applications.

The unique capabilities of the femtosecond laser pulses are due to the nonlinear nature of the absorption of the pulses by the biological tissue. Optical breakdown of a material occurs when the electron density localized to the area of laser absorption exceeds a critical value [1, 57]. Nanosecond laser pulses achieve this process through single photon absorption, as the pulse peak power is not high enough to induce non-linear absorption. Alternatively, in the case of femtosecond

laser pulses, optical breakdown is achieved through the non-linear process of multiphoton absorption, when a material is transparent and with no absorption at the wavelength of the femtosecond pulses. In this case, multiple photons with lower per photon energy are required to excite an electron from one energy state to another compared to the single photon absorbed in the alternate situation. Water is widely accepted as a model for tissue during laser-tissue interaction [60]. During multiphoton absorption, enough photons must be simultaneously absorbed to exceed water's assumed energy band gap of 6.5 eV. Therefore, with a femtosecond pulse centered at 800 nm, which has photons of 1.55 eV, 5 photons must be absorbed to surpass the tissue energy band gap. The reduced energy needed to induce electron excitation is what enables reduced levels of collateral damage observed during femtosecond laser pulse interaction with biological tissue compared to nanosecond pulsed lasers, as there is less energy delivered to the target material [1, 51, 61–63]. The freed electrons, after multiphoton absorption, can then absorb incoming photons reaching a higher energetic state in which they collide with and ionize an atom, in turn releasing more free electrons that then free more electrons in the nonlinear process known as avalanche ionization. Once the electron density hits a critical level, plasma is generated and ablation occurs [1, 57]. The spatial resolution of ablation by femtosecond pulses is governed by the spatial profile of the resulting electron density, as opposed to the irradiance profile of the beam [60]. With the microscope objective used in this work, the focal spot is approximately 800 nm and the axial depth of focus is 0.53 μm [61, 64, 65]. It is only within the enclosed focal volume that the femtosecond pulses surpass the threshold to induce nonlinear

ionization. Any photons at any other point in the beam path, whether before reaching the focal region or if they pass through without participating in the multiphoton nonlinear absorption, will be unable to surpass the optical breakdown threshold and will have no noticeable effect on the material [60]. The process of femtosecond laser pulse induced plasma mediated ablation is a powerful ablative method: efficient, reproducible, and with known thresholds.

The energy delivered to the tissue through single photon or multiphoton can have serious disruptive effects. As previously discussed, thermal disruption is a very serious concern, particularly with longer pulse lasers as the pulse exceeds the thermal relaxation time [1]. In this situation, thermal energy is diffused within the tissue, leading to collateral damage in a significant spatial region around the point of laser delivery. Shock wave generation and cavitation bubble formation are two other disruptive effects that must be considered during laser energy deposition [1, 3, 51, 57, 63]. The kinetic energy of the free electrons created during the multiphoton ionization is converted into the propagating shockwave. If the ionization process occurs in a liquid environment, the vaporization of the local volume creates a cavitation bubble. Both the shockwave and cavitation bubble are sources of mechanical stress, and potentially damage, on the tissue. However, both physical disruptions can be avoided if appropriate laser parameters are chosen for plasma-mediated ablation by an ultrafast laser pulse, in turn eliminating the collateral damage characteristic of other laser systems.

1.4 Thesis Scope

The main objective of this research is to demonstrate the ability of femtosecond pulses to ablate drusen caused by AMD. The specific aim is to show that if femtosecond laser pulses are delivered to sub-RPE drusen-like deposits in an experimental model of AMD, then the deposits will be accurately and precisely ablated with no collateral damage because of the unique non-linear, multiphoton absorption of the femtosecond laser pulse-tissue interaction. Figure 1.8 depicts the proposed therapeutic situation with femtosecond laser pulses delivered to the sub-RPE drusen deposits where multiphoton absorption would lead to isolated ablation only at the point of focus of the laser. Soft drusen are a known risk factor for late, more severe, AMD. Removing the drusen, particularly if the VEGF cytokine is concentrated in the drusen and stimulating the neovascularization, could significantly reduce the risk of progression and further vision loss [13, 15]. This thesis also includes the design and fabrication of a prototype device for pulsed beam delivery to the retina. Preliminary results from the study of laser-tissue interaction between femtosecond pulses and drusen-like deposits will provide a better understanding of the potential of laser systems as a treatment for AMD. In future studies, the preliminary results herein can be built upon in the development of a preventative treatment for AMD.

This thesis consists of five chapters outlining the development of a device for laser beam delivery to the retina, the development of a cell culture model of dry AMD, and the results of femtosecond laser pulse delivery to the cell culture model.

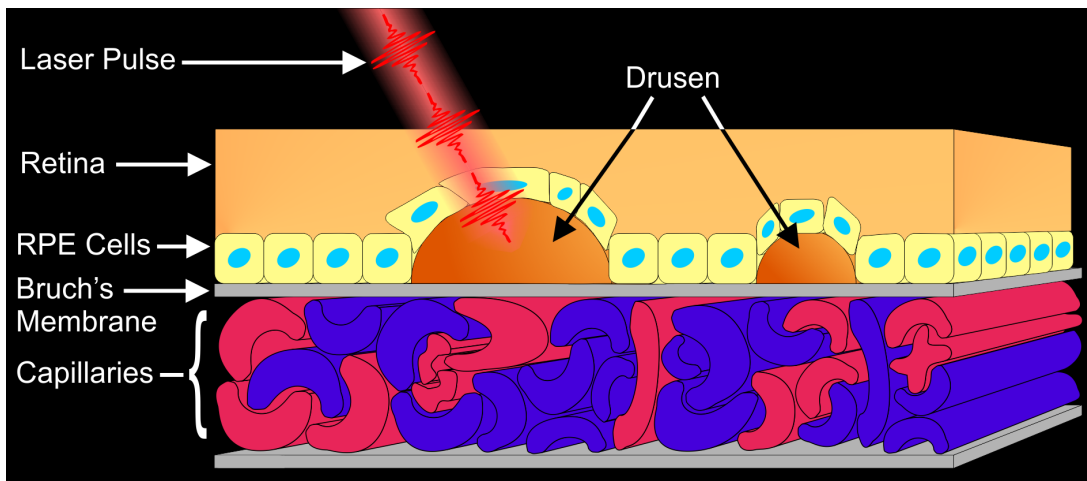


Fig. 1.8: Depiction of proposed femtosecond laser assisted treatment for AMD. The only laser-tissue interaction will occur at the focal point of the laser beam, which can be precisely applied to the sub-RPE drusen. The drusen are laser ablated without collateral damage to any of the important surrounding tissue.

Chapter 2 describes the design and fabrication of a device for the delivery of femtosecond laser pulses to the retina. This prototype system can be used during the next steps in this research, including femtosecond laser pulse enabled ablation of drusen in human donor eyes containing AMD drusen or a clinical trial. Additionally, the characterization of the ablation threshold of fresh ARPE-19 cells plated on standard glass dishes is outlined in Chapter 2. Many trials were performed with varying average power level and exposure window duration to determine the optimal threshold for femtosecond laser pulse ablation of ARPE-19 cell culture samples.

In Chapter 3, the development of a novel ARPE-19 cell culture model mimicking aspects of dry AMD is reported. There are a limited number of research models of dry AMD available, and none of the models currently available were deemed suitable for this research. Therefore, a novel research model was created to satisfy the requirements for this project. A cell culture model with drusen-like sub-RPE deposits using ARPE-19 cells was successfully created. The key requirements for the experimental model were the presence of sub-RPE deposits, physiology relatively comparable to that of the human retina, and system compatible with the equipment for the laser beam delivery.

Chapter 4 briefly describes the microscope-coupled system for the delivery of the laser beam. Furthermore, the results of the femtosecond laser pulse interaction with the sub-RPE drusen-like deposits is reported. Images demonstrating both the successful and unsuccessful isolated ablation of sub-RPE deposits are presented. In the successful case the deposit is removed from the field of view while the overlying

ARPE cells are left unaffected. In the unsuccessful example the laser pulse interaction is not isolated to the deposit and collateral damage to the overlying cell layer is visible. Evidence to disprove the laser over-powering and photobleaching the fluorescent stain used to identify the deposits is also presented.

The research presented within this thesis is summarized in Chapter 5. Chapter 5 also examines the future prospects for this research.

Chapter 2

Femtosecond laser pulse coupling to a slit-lamp

2.1 Introduction

Since almost immediately after their invention, lasers have been considered an instrumental tool in the field of ophthalmology [1]. A variety of different types of lasers have been used to treat a plethora of ocular conditions using such protocols as photocoagulation, photodynamic therapy, and photobleaching [48, 63]. However, most such laser-assisted treatment protocols that use continuous wave or lasers pulsed on the nanosecond to microsecond scale have been contested in the intervening years. During the treatment protocol, the previously available devices induce collateral damage to tissue surrounding the desired target leading to detrimental side effects that far outweigh the therapeutic result [51, 66]. However, such is not the case with certain ultrafast laser pulse profiles, particularly femtosecond laser pulses with appropriately set pulse parameters, which have recently become a promising subject of research for biomedical applications [1]. The physics that distinguish the femtosecond laser-tissue process from that of other laser

systems was outlined in Chapter 1. Probably the most ubiquitous example of laser assisted ophthalmology, laser-assisted in situ keratomileusis (LASIK) surgery is one of the few application in the field that has already adopted the femtosecond laser system [2]. Additionally, most ophthalmic systems that do harness the unique capabilities of femtosecond laser pulses target afflictions on the anterior surface of the eye. A femtosecond laser pulse is an excellent platform to target and interact with the posterior pole of the eye. With an appropriately selected wavelength, power density, and spot size, the penetration depth can be quite deep and the laser pulse-tissue interaction phenomena will only occur at the focal point of the beam. To harness the unique properties of femtosecond laser pulses, first a tool with which to administer the treatment beam to the target tissue is required.

2.2 Equipment

One specific aim of this thesis is the creation of a prototype of a clinical tool that employs the unique characteristics of femtosecond lasers for the treatment of ocular conditions. Many consultations were had with practicing retinal surgeons to understand the difficulties of retinal laser surgery and what would be required of such a device. It was determined that the device would be built around a slit lamp ophthalmoscope. The optics of this system of visualizing the retina are, relatively speaking, easy to access and alter or tailor as need be. Additionally, the slit lamp is that base for most current retinal laser systems, providing two important benefits. First, retinal surgeons are already trained on and comfortable with using a slit lamp

laser delivery system. Secondly, slit lamps were available for purchase with beam delivery optics already attached.

The final prototype that was assembled is fundamentally two base parts: a slit lamp ophthalmoscope and an articulating beam delivery arm. A few minor adjustments and custom connectors had to be machined but eventually a prototype clinical tool for the femtosecond ablation of sub-retinal deposits was complete.

2.2.1 Slit lamp

The slit lamp was purchased online and arrived with a beam delivery mirror mechanism already mounted to the top. However, none of the electrical circuitry housed within the slit lamp was functional. Therefore, the entire circuit was mapped and reverse engineered, and a replacement circuit design was mapped out and then soldered (Fig 2.1). The new circuit was installed in a vented box, with a fan to keep internal temperature in an acceptable range, and mounted under the slit lamp table. Power was restored to the diagnostic light within the ophthalmoscope, including dimming capabilities. Additionally, there was a shutter mechanism on the beam delivery mirror housing that when blocked would introduce some filter glass into the eye path of the medical professional and illuminate a small, cautionary “laser in use” LED. This circuit was also resorted, as seen in Fig. 2.2, and new 800 nm absorbing glass was purchased and housed within the shutter to ensure proper filtration of the beam of our laser, protecting the retinal surgeon from the powerful beam.

2.2.2 Articulating arm

The articulating arm was purchased from a decommissioned Ar-ion laser system. The only alteration made to the articulating arm itself was that the mirrors in

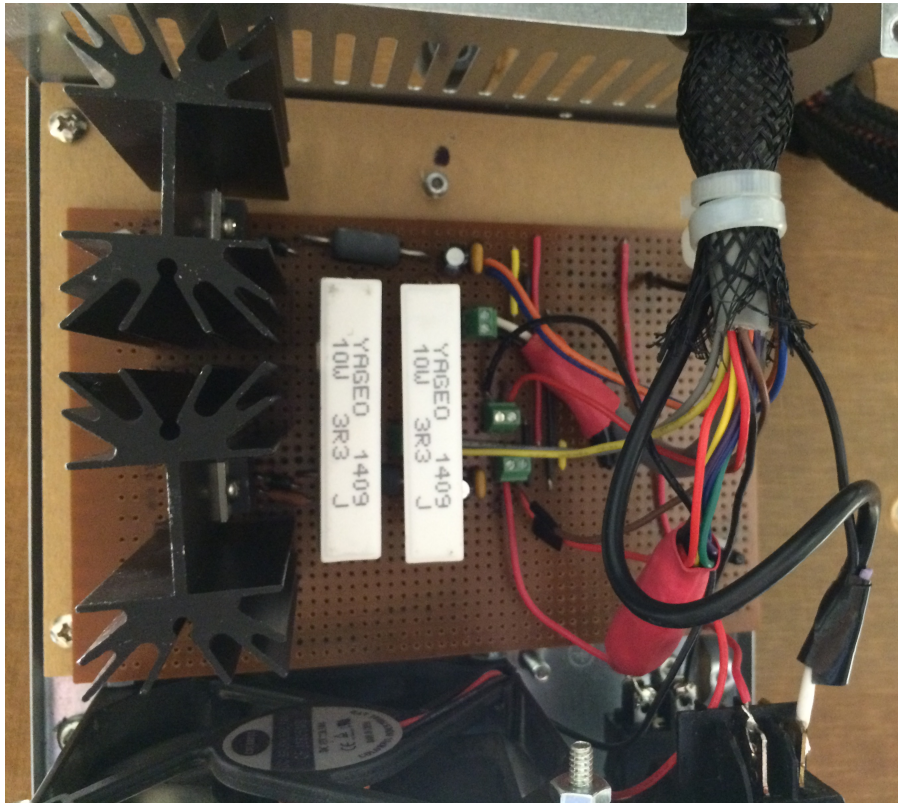


Fig. 2.1: The completed power circuit for the slit lamp. A refurbished computer fan maintains an adequate operating temperature for the heat sink laden resistors.

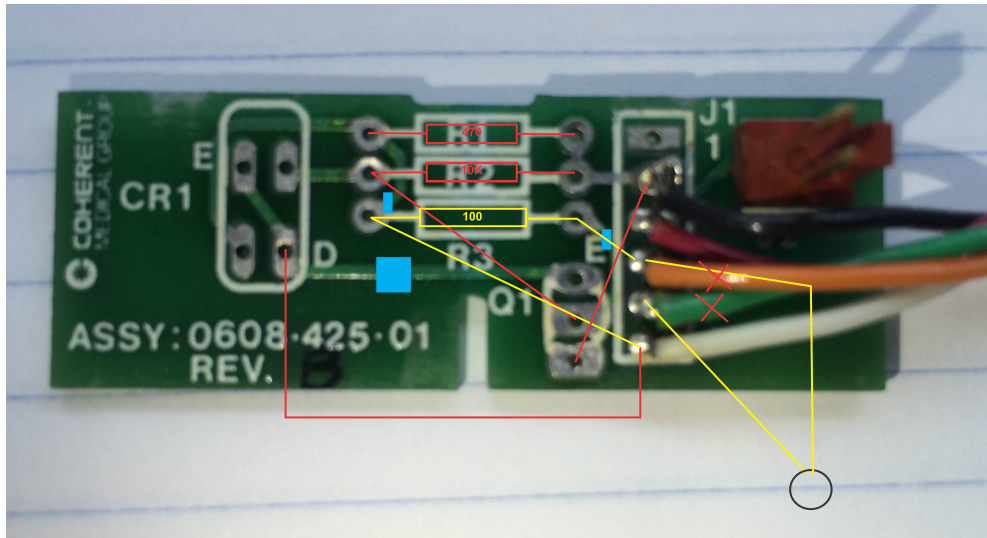


Fig. 2.2: Redesigned safety circuit for the beam-blocking shutter housed in the binocular chamber of the slit lamp device.

all of the junctions were removed. New silver mirrors that are optimized to reflect the femtosecond pulses laser beam the system is designed around were purchased. A few custom pieces were machined to anchor the arm in place on an optical breadboard and direct the beam path into the articulating arm opening. An important adapter was a piece to hold the opening of the arm perfectly perpendicular and mount an aperture onto the opening for assistance during laser alignment (Fig 2.3).

2.2.3 System integration

As most of the major pieces for the device were repurposed, a few small changes were necessary to make it function as a single unit. For example, as mentioned previously the filter glass in the shutter that snaps in front of the surgeon during laser administration had to be replaced. The new filter glass is appropriate for 800 nm, the wavelength at which the femtosecond ablation investigations will occur; as opposed to the wavelength that had been used in the therapeutic protocol the slit lamp was initially intended for. Additionally, whatever the previous laser protocol purpose had been, it used a laser fiber to introduce the beam into the mirror mechanism on top of the slit lamp. Using a fiber for our femtosecond beam delivery is out of the question as it significantly distorts the pulses in the fiber and the unique femtosecond interaction properties are lost. A condensing lens of appropriate focal length was spliced in between the articulating arm and slit lamp mirror junction. The lens now focused the beam arriving in the articulating arm to a point at the aperture of the mirror mechanism, making the optical system perform as if it was still receiving a fiber source.

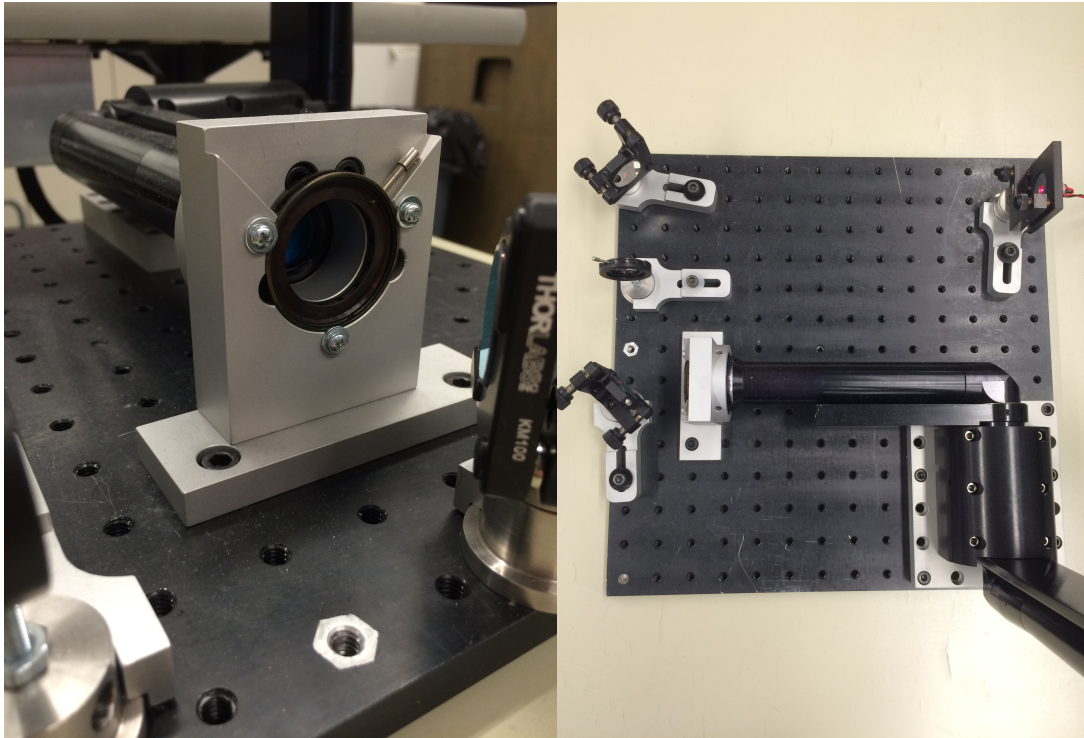


Fig. 2.3: Custom designed and machined anchor for the horizontal section of the articulating arm. The Aperture is mounted on the front of the arm opening to aid in alignment procedures. The right image shows a diode laser beam entering the articulating arm pathway after successful alignment.

2.2.4 Future work

The fully assembled retinal laser surgery beam delivery tool is seen in Fig 2.4. The articulating arm is attached to the slit lamp via the custom adapter that houses the required condensing lens. The diagnostic white light and red laser light are visible on the blue target stuck to the dummy head. Although this prototype is a great starting point, there is a lot that can be done, and should be done, before this device is available to clinicians.

The next step in this prototype would be to motorize the control of the mirror that directs the treatment beam. Currently, the mirror positioning is controlled via a very imprecise joystick. The accuracy and precision of the treatment protocol would immediately and significantly be improved if the control of the beam direction was automated via motors. Secondly, future work could be done to install a system to identify and target points for ablation using a computer. Using an image feed of the patient's retina, as opposed to looking through the binoculars of the slit lamp device, the retinal surgeon could map out, and even save for records, a precise and accurate treatment plan on the video feed from the patient's retina. The computer would then automatically administer the femtosecond pulses in the treatment map using the motorized mirror control. Finally, the same video feed the operator uses to pattern the treatment protocol into the computer, could also provide a safety feedback loop. An image processing software could register and constantly follow landmarks on the retinal video. The computer would then prevent the laser being exposed to any part of the eye that was not explicitly labeled as a target during the treatment plan patterning. Fragile parts of the eye could be excluded and hard coded to disengage

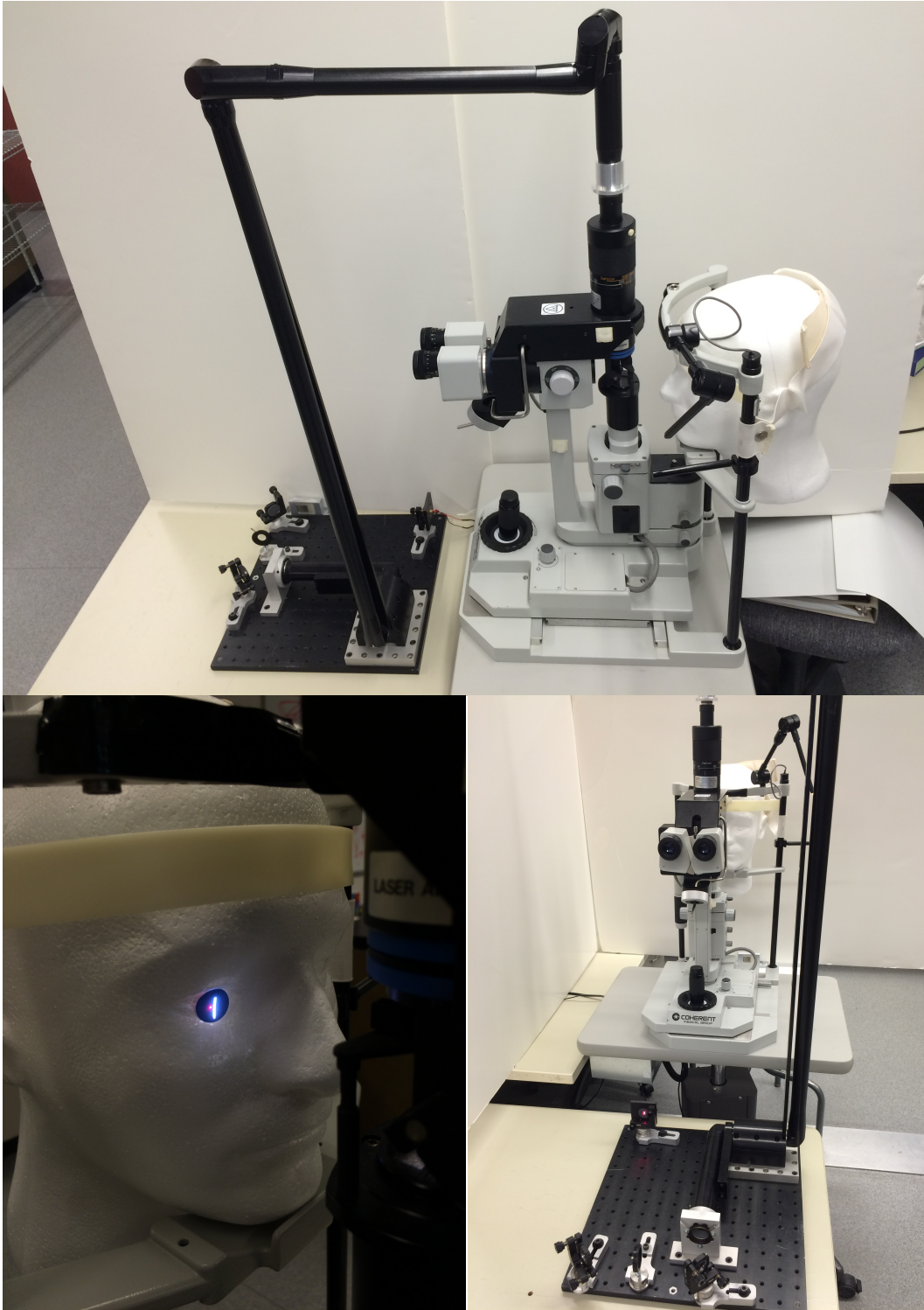


Fig. 2.4: Fully assembled prototype of femtosecond retinal surgery device. The images show the articulating arm connected into the slit lamp mirror mechanism. The condensing lens is housed in the silver adapter between the black arm and black mirror mechanism. The diagnostic white light and red “treatment” beam can be seen on the blue target mounted on the dummy.

the laser should it move in front of the beam path. This would ensure precise, machine correction for the constant and subtle movements of the patient's eye during the procedure. Any or all of the above suggestions are important future works that will continue to improve the femtosecond retinal surgery device constructed during this project.

Chapter 3

Engineered model of dry AMD that develops drusen-like sub-RPE deposits

3.1 Motivation

In addition to the design and fabrication of a system for laser delivery to the retina as discussed in the previous chapter, the main objective of this project is to demonstrate the isolated ablation of drusen using femtosecond laser pulses. However, for this investigation to be executed required the availability of an effective and appropriate model system. There are very few experimental models of dry AMD available, and none of those fit the constraints of this project. The model needed to be physiologically comparable to the human system, to display drusen-like sub-RPE deposits, to be able to fit on and be visualized by a microscope, and have components available to ground level researchers. At the outset of this project, no such experimental model was available. As such, a novel cell culture experimental model was developed to solve this issue. The following chapter outlines the currently available research models, followed by the description of the

work done to develop the custom dry AMD experimental model used in the femtosecond laser ablation work.

3.1.1 AMD animal models

Many animal models of AMD exist. However, most animal models are tailored to display the symptoms of wet, late AMD [28, 67]. Of the few experimental systems that mimic early AMD, only a very small margin exhibits the development of sub-RPE deposits. The composition of the induced sub-RPE deposits differed from that of naturally occurring drusen *in vivo* in human subjects. And none of the experimental systems that mimic the development of sub-RPE deposits, specifically the most popular model of mice, possess a macula [68, 69]. As explained in Chapter 1, the macula is the central region of the retina with a dense population of cone photoreceptors [10]. It is the macula that is the region affected by degeneration during AMD. Thus, it is unreliable to make inferences for what would happen in humans from the results of such an animal model. The significant physiological and pathological differences between what is seen in human patients and the available animal models of early AMD make the animal models an unacceptable choice for this study.

3.1.2 Primary cells vs. cell lines

The best choice for experimental model is one that is human derived. However, there are many barriers that make using human derived systems very difficult, particularly for a project exploring proof of concept results. The best experimental system for a potential treatment for AMD would be individuals currently suffering from said condition. But this constitutes a clinical trial and there

are many, many required steps prior to this stage. The requirements for clinical trial are very complicated but include copious amounts of proof of concept and therapeutic potential. Thus, for this investigation human subjects are out of the question. The next option would be to obtain enucleated eyes from deceased individuals that have the symptoms of early AMD; mainly, drusen are already present under the retina and can be targeted during experimentation. There is a strict system of approvals for researchers to obtain human donor tissue, which again includes demonstrated proof of concept with preliminary results. Although human tissue with AMD already present is unattainable for the purposes of this study, another option would be to use primary cells induced to develop sub-RPE deposits. Primary cells describe an experimental cellular system that is created using cells harvested and then proliferated directly from a sample of the desired experimental tissue. Investigations into retinal conditions have previously used primary cells harvested from a retina or pluripotent stem cells induced to form the necessary retinal cells. Sources of primary cells are also tightly regulated, and expensive to work with, thus presenting another hurdle for experimental models available to our investigation. The opposite of primary cell lines are non-primary cells lines, referring to a continual cell line that either spontaneously or through artificial means proliferates indefinitely. Although not the most biologically reliable cell culture option, cell lines are widely available and very easy to handle. A potentially suitable experimental model for this investigation is one using non-primary human cell line as they are easily attainable, relatively inexpensive, and straightforward to work with.

3.1.3 Purpose of this study

The purpose of this study is to create a suitable experimental model of early AMD that displays drusen-like sub-RPE deposits. Additionally, it is important that the induced drusen-like deposits share the fundamental biological composition as naturally occurring drusen. This investigation was necessary to proceed to exploring the capabilities of femtosecond laser pulses for the treatment of early AMD. After exploring a few unsuccessful attempts at developing an experimental model, including artificial drusen introduction to dissected porcine retinas, a method was found that satisfactorily replicated early AMD drusen formation. A novel cell culture model of early AMD was created using a spontaneously arising immortalized RPE cell line known as ARPE-19 [70]. The ARPE-19 cells were seeded onto porous membranes and developed sub-RPE deposits after five weeks of incubation. Using both confocal and transmission electron microscopy (TEM) the sub-RPE drusen-like deposits were shown to share multiple components with naturally occurring drusen deposits.

The potential applications of the novel ARPE-19 cell culture model are numerous. Age-related macular degeneration is the leading cause of blindness in the developed world and does not have a cure [5]. The cell culture model described herein utilizes an immortalized cell line. While human derived, it is far easier to handle and less costly than primary cells. This opens the door for far more experimental investigations into treatment options for AMD as the cost and cellular biology requirements are lessened. Given the prevalence of this disease, the more

investigations into effective treatments for AMD, the better for both the healthcare system and quality of life of those afflicted by this condition.

3.1.4 Preliminary model attempts

Prior to the successful development of the ARPE-19 model that was used in the femtosecond laser pulse-tissue investigation, two alternative experimental models were investigated. An initial attempt at using ARPE-19 cells to mimic early AMD was unsuccessful because of a number of limiting factors. ARPE-19 was chosen as the cell line as Amin et al. [71] had previously been successful in inducing sub-RPE deposit formation using that particular cell line. In their investigation, cells grown in the presence of bovine serum albumin (BSA) had more substantial deposit formation when compared to cells grown solely in typical cell culture medium. However, not until after the initial incubation period of the experimental cell group during our investigation was it discovered that BSA can inhibit apolipoprotein E (ApoE) production in ARPE-19 cells [72]. This is significant because ApoE has been identified as one of the major drusen components [36–38], and it was one of the two components that we stained for and used to identify drusen-like deposit formation in the samples. Thus, in the second attempt at ARPE-19 experimental models, BSA was not introduced to the cell culture medium during sample incubation. Additionally, when the first ARPE-19 samples were ablated with the femtosecond laser pulses, a substantial amount of absorption within the background was observed. The porous polyethylene terephthalate (PET) membranes on which the cells were seeded absorbed and were ablated by the laser pulses. Therefore, it would be impossible to attempt an investigation into the isolated ablation of sub-

RPE deposits on this membrane without the interference of the membrane ablation. A new brand of porous membranes that were instead made out of mixed cellulose ester and would not interact with the laser were obtained for the second attempt at ARPE-19 cell culture model creation.

During the incubation period of the second attempt at an ARPE-19 cell culture model, alternative avenues for AMD simulating targets investigated. An option that was pursued for a brief time was a system of engineering artificial drusen deposits and then manually introducing them to the sub-RPE space of an enucleated and isolated choroid-retina structure of a porcine eye. This experimental model, while feasible, presented a great many difficulties stemming from the required intricacy. Though the lipid and proteome composition of drusen is a largely researched area, the exact formula of drusen is yet to be determined. A wide range of different proteins and lipids have been identified, and different scientific investigations found slightly different ratios and populations of said components [34, 36–38]. Thus, it proved difficult trying to determine what substance to use in creating the artificial drusen that was easily obtained and ensured the simulated drusen mimicked naturally occurring drusen in shape and composition [73, 74]. Another point of concern was the method in which the artificially engineered drusen, once successfully created, would be introduced to the sub-RPE space of the porcine sample. One technique investigated was micro-pipetting the drusen deposit below the RPE cells. The variety of complex techniques required to create the experimental model made it a poor choice for this project, as it required mastery of porcine ocular dissection, lipid droplet fabrication, and micro pipetting of small

deposits into delicate tissue. When the second round of ARPE-19 experimental samples was shown to be successful, the potential porcine drusen model was discarded.

3.2 ARPE-19 cell culture model

3.2.1 Experimental Methodology

3.2.1.1 Cell Culture

ARPE-19 cells were initially seeded 120,000 cells/well onto 0.45 μm pore porous mixed cellulose ester membranes (Millicell-HA PIHA03050; EMD Millipore, Billerica, MA, USA) for confocal microscopy imaging or 0.40 μm pore porous polyethylene terephthalate membranes (Falcon 353090; Corning Inc., Corning, NY, USA) for TEM imaging. The pores are randomly oriented throughout the membrane. The cells were grown in DMEM F12 media supplemented with 10% Fetal Bovine Serum, 2 mM L-glutamine, and 1X Penicillin/Streptomycin that is changed twice a week. Cells were incubated at 37°C and 5% CO₂. Experimental cells were grown for a minimum of five weeks and control cells were grown for less than 3 days, for comparison.

3.2.1.2 Confocal Microscopy

To prepare the cells, media was decanted and the cells were rinsed with phosphate-buffered saline (PBS). Fixation was achieved by the addition of 4% paraformaldehyde in PBS, pH 7.4 for 15 minutes at room temperature. Following three washes with PBS the cells were subsequently permeabilized through

incubation in 0.2% Triton-X in PBS for 10 minutes. After three more PBS washes, cells were left in PBS until staining.

For ApoE antibody staining, nonspecific blocking required incubating the cells for 30 minutes in 1% Bovine Serum Albumin (BSA) and 22.5 mg/mL glycine in PBS+ 0.1% Tween 20 (PBST). This was followed by overnight incubation at 4°C with the primary antibody (Goat polyclonal Anti-Apolipoprotein E, AB947; EMD Millipore, Billerica, MA, USA) diluted to 1/1000 in 3 mL of 1% BSA in PBST. The solution was then decanted and the cells were rinsed three times with PBS. The secondary antibody (Donkey Anti-Goat IgG H&L – Alexa Fluor 488, AB150129; Abcam, Cambridge, UK) was diluted to 1/500 in 1% BSA in PBST. Incubation was then performed for one hour, in the dark, and at room temperature, followed by three more washes in PBS. Cholesterol staining used filipin (F9765; Sigma-Aldrich, St. Louis, MO, USA) dissolved in DMSO added to the well to a final concentration of 100 µg/mL. After 1 hour of incubation, the solution was decanted and the cells were washed three times. Filipin staining was performed concurrently with secondary antibody staining where dual staining was called for.

Samples were mounted onto glass slides with 1.5 glass coverslips for confocal microscopy examination. The porous membranes were excised from the plastic well using a scalpel and the membrane was placed on the slide with the cell side closest to the cover slip. A drop of Prolong Gold Antifade Mounting Reagent (P10144; Invitrogen, Carlsbad, CA, USA), with or without additional DAPI staining, or Permount (SP15-100; Thermo Fisher Scientific, Waltham, MA, USA), depending on the requirements of the imaging session, was placed on the slide

above and below the membrane. The slide was left to cure for a minimum of 2 hours and up to overnight. For visualization, excitation of ApoE was at 488 nm and filipin was excited at 405 nm.

3.2.1.3 Electron Microscopy

Samples were prepared for investigation by transmission electron microscopy similarly to the method outlined by Burles et al. [75]. Briefly, cells are grown on PET porous inserts from Falcon before fixation. The fixative was added to the cells and left for an hour at 37°C. Unlike the Burles et al. [75] protocol, propylene oxide was not used in the preparation of our samples. After cell blocking to improve contrast, cells were embedded in Spurr's resin and polymerized at 65°C for 24 hours. Samples were then sectioned with a Leica UC7 ultramicrotome (Leica Microsystems, Inc., Wetzlar, Germany) perpendicularly to the cell layer growth and membrane. Sections were stained with 2% uranyl acetate and Reynolds' lead citrate then imaged with a Hitachi H-7650 transmission electron microscope (Hitachi High-Technologies, Minato-ku, Tokyo, Japan) and a 16 megapixel TEM camera (XR111; Advanced Microscopy Techniques, MA, USA).

3.2.2 Results

Confocal microscopy of ARPE-19 cells cultured following the above methodology allowed us to identify the presence of two significant drusen components: ApoE and cholesterol. ApoE is a protein that binds to cholesterol lipoproteins for transport throughout the body, including across Bruch's membrane, and it is thought to be a source of lipid accumulation in the basal region of RPE [43, 76, 77]. Experimental samples that were grown for a minimum of five weeks (5-

Week) were compared to cells that were incubated for only a few days (3-Day). Figure 3.1(a) shows the experimental sample of 5-Week cells, with several bright spots indicating the sizable sub-RPE deposit accumulation visible through the cell layer. For comparison, a sample of 3-Day cells is shown in Fig. 3.1(b). The 3-Day sample in Fig. 3.1(b) had no regions of fluorescence strength comparable to the deposits in the 5-Week sample. The sub-RPE deposits in the 5-Week samples were non-uniformly distributed throughout the whole field of view. Deposits varied in size, with the largest observed to be approximately 20 μm . A MATLAB script was created to apply a mask to the confocal images to determine pixel volume fraction of the image that is deposits. An appropriate threshold value was selected such that only areas of deposit accumulation were filtered through the mask. The ratio of deposit pixels to the total pixel count of the image was then calculated. Applying the mask to images of 5-Week and 3-Day samples enable quantitative comparison of deposits in the respective samples. Figure 3.2 shows an example of a 5-Week and 3-Day confocal image, Fig. 3.2(a) and Fig. 3.2(c) respectively, and the resulting black and white image after filtering for deposit accumulation, Fig. 3.2(b) and (d). When filtered through the mask to quantify the relative area of deposit accumulation within the confocal image, 5-Week samples were found to have an average pixel volume fraction of accumulated material six times that of 3-Day samples.

Cholesterol is another important component of naturally occurring drusen; [36, 37, 78] we used the fluorescent stain filipin to identify any esterified cholesterols present in our sample [78, 79]. Figure 3.3 shows the 5-Week cells visualized with filipin staining; the circles in the figure indicate a number of

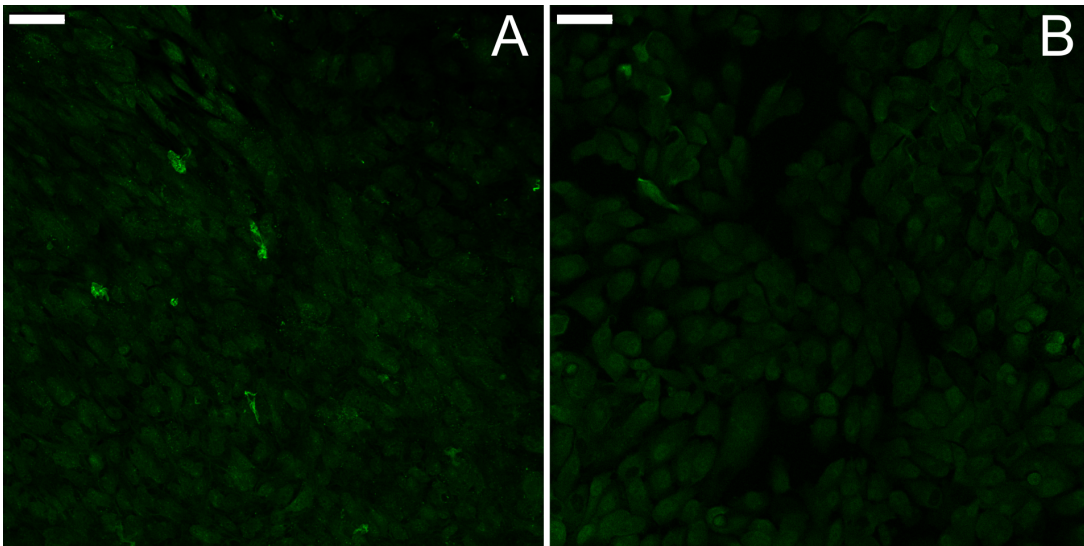


Fig. 3.1: Confocal microscopy images with ApoE antibody staining of the two different culture samples. (A) Shows the experimental sample of ARPE-19 cells grown for five-weeks. (B) Shows the control sample of cells grown only until confluence. The control sample in (B) shows no deposit immunoreactivity compared to (A). (Scale bars, 50 μm in A and B.)

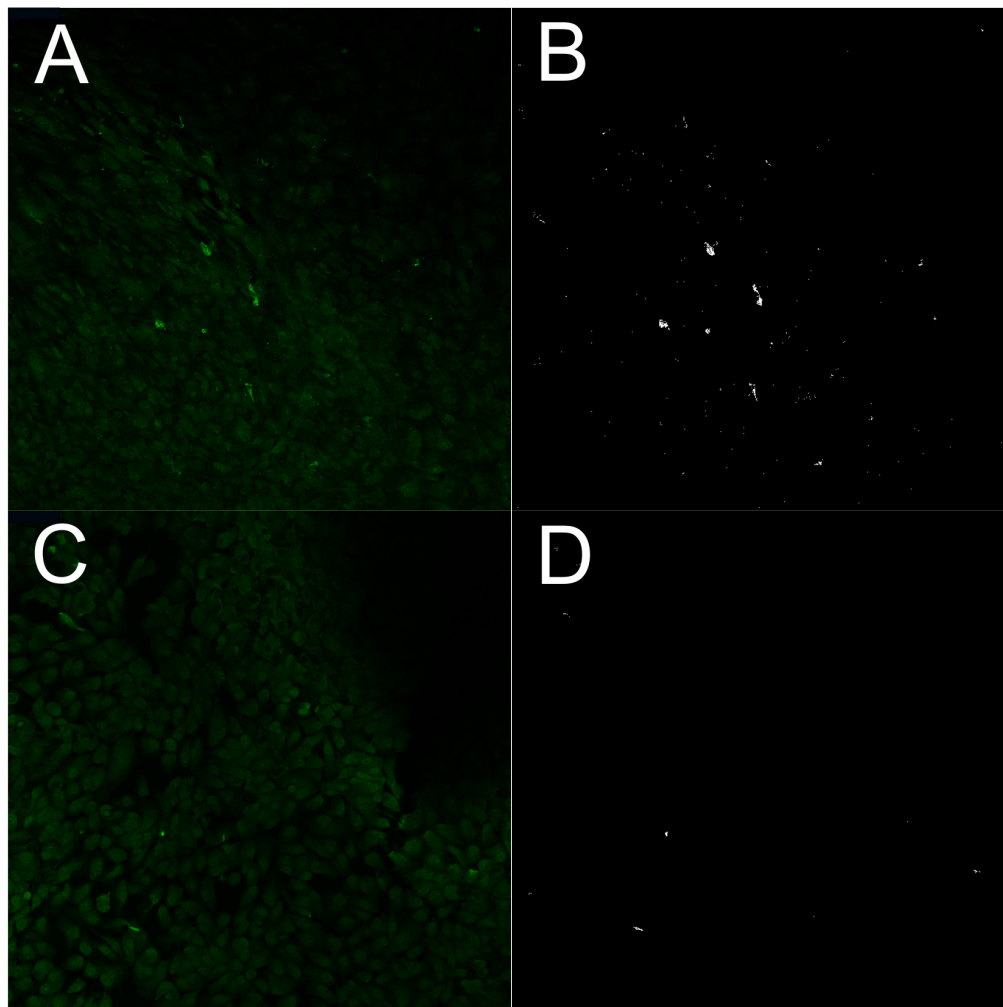


Fig. 3.2: Confocal microscopy image of 5-Week and 3-Day ARPE-19 cell culture samples and the filtered image after using a mask to isolate deposit accumulations. (A) and (C) are the original confocal image of a 5-Week and 3-Day sample, respectively. (B) and (D) are the images obtained after applying a mask created in MATLAB to isolate pixels of deposit accumulations. The pixel threshold mask values quantitatively demonstrated the experimental sample in A/B shows more deposit accumulation than the control sample in C/D.

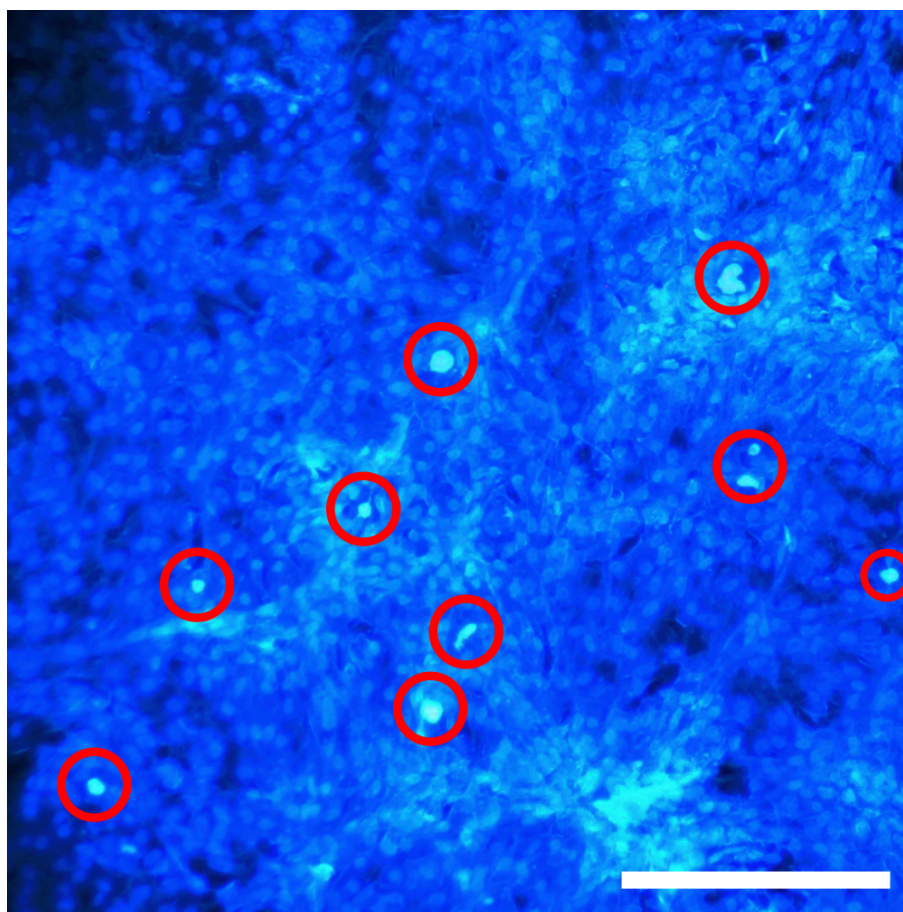


Fig. 3.3: Confocal microscopy image of a 5-Week ARPE-19 sample treated with filipin. The circles indicate a number of cholesterol rich sub-RPE deposits stained intensely with filipin. (Scale bar, 500 μm .)

cholesterol rich sub-RPE deposits. A similar number of sub-RPE deposits were observed with either filipin or ApoE staining. Additionally, some sub-RPE deposits observed in this cell culture model stain simultaneously for ApoE and cholesterol, as seen in Fig. 3.4 [36–38]. The circle in Fig. 3.4(a)-(c) highlights the same sub-RPE deposit in all three images. Figure 3.4(a) is a confocal microscopy photo of a 5-Week sample dually stained, with the two fluorescence channels overlaid. The teal color of the deposit in the image indicates the co-localization of both the protein and the lipid component within the deposit. Figures 3.4(b) and 3.4(c) separate the ApoE stain channel and filipin stain channel, respectively. The identification of both protein and lipid constituents in deposits beneath the cell layer is analogous to sub-RPE drusen *in vivo*.

Amin et al. [71] previously investigated an *in vitro* sub-RPE deposit cell model with ARPE-19 cells and reported four different types of sub-RPE deposit structures, labeling them: “fibrillar, condensed, banded, and membranous”. Johnson et al. [80] used primary RPE cells in their culture model and described “nonmembrane-bounded conglomerates of small osmophilic particles, and membrane-bounded, multi-vesicular structures.” Through TEM investigation, we observed deposits similar in structure and appearance to the “fibrillar, membranous, and banded deposits” reported by Amin et al. [71]. Comparison of a 5-Week sample and a 3-Day sample through TEM imaging revealed sub-RPE deposits only in the 5-Week sample. Figure 3.5 shows the different deposit structures we observed through TEM. In Fig. 3.5(a), a condensed deposit is highlighted within the circle. Multiple membranous deposits are visible in the circled region of Fig. 3.5(b). The circle in

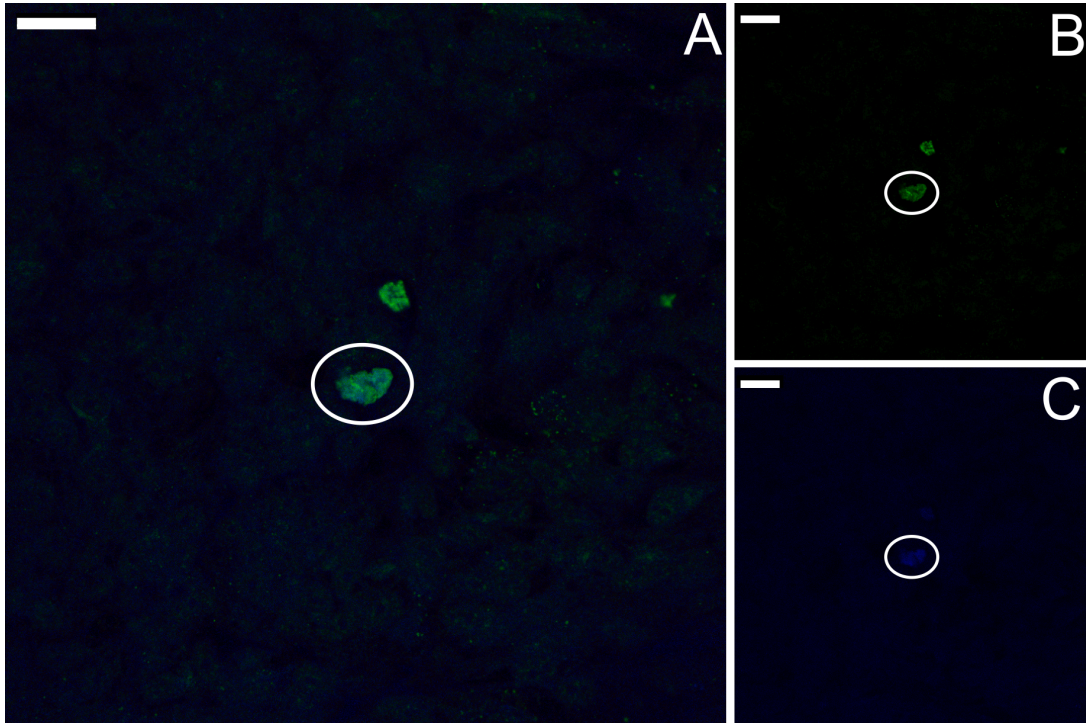


Fig. 3.4: Confocal microscopy image of a 5-Week ARPE-19 sample stained simultaneously with ApoE and filipin. The circle in each image outlines the same sub-RPE deposit in each channel. (A) Shows both the ApoE and filipin channels overlaid indicating the co-localization of ApoE and cholesterol in the deposit. For clarity, the individual stain channels are separated to further emphasize the co-localization with ApoE in (B) and filipin in (C). (Scale bars, 25 μm in A, B, and C.)

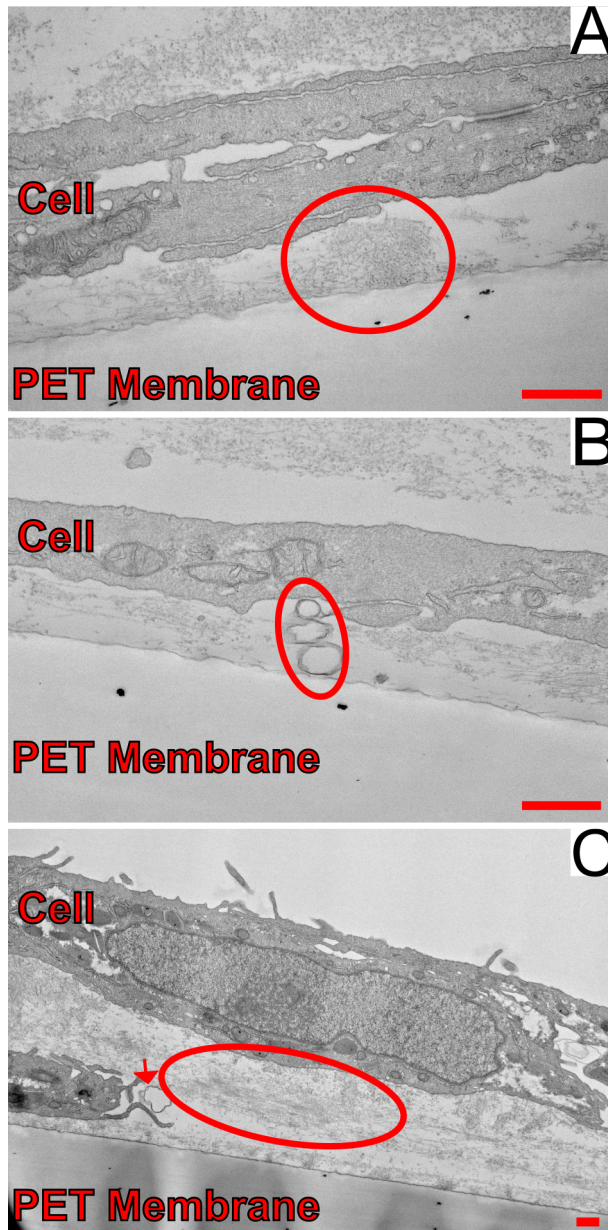


Fig. 3.5: TEM images of sub-RPE deposits formed in a 5-Week ARPE-19 cell culture. (A) An area of condensed deposit formation (*circle*). (B) Examples of membranous deposits (*ellipse*). (C) Shows an area of fibrillar deposit formation (*ellipse*) as well as highlighting a membranous deposit also visible in this area (*arrow*). The cell layer and porous membrane are labeled in each image. (Scale bars, 500 nm in A, B, and C.)

Fig. 3.5(c) outlines an area of fibrillar deposit build-up. Additionally, the arrow in Fig. 3.5(c) points to a membranous deposit also visible in the same image. The RPE cell layer and porous membrane are labeled in Fig. 3.5(a)-(c). The distance between the cell layer and the porous membrane varied throughout the sample, as shown in Fig. 3.6. In areas where deposit formation was observed, the cell layer was raised up to 2.4 μm above the membrane (Fig. 3.6(a)). Three regions of fibrillar deposits are outlined by the dotted ovals in Fig. 3.6(a). In this image, the cell layer has been pushed several microns above the porous membrane due to the accumulated debris. In contrast, in deposit free areas the cell layer is only 245 nm above the membrane, as seen in Fig. 3.6(b). TEM images revealed cellular material deposited within the 0.4 μm diameter pores of the membrane (Fig. 3.7). Membranous deposits, appearing similar to cellular blebs, are lodged in the pores of the membrane, visible in Fig. 3.7(a) and 3.7(b). Figure 3.7(a) has a single pore visible, with three membranous deposits. For clarity, the insert provides an enhanced view of these deposits. Similarly, in Fig. 3.7(b) two pores are visible and a single deposit is lodged within one of the pores, with an enhanced view of the deposit in the insert.

Select 5-Week samples were trypsinized, to remove the ARPE-19 cell layer, prior to undergoing the ApoE confocal stain protocol to ascertain whether the deposits may indeed be lodged within the pores of the membrane. Figure 3.8 demonstrates that after removing the cell layer with trypsin, large deposits were still present on the membrane. The deposits observed on the insert after the trypsin treatment were comparatively large given the variety of deposit sizes observed in

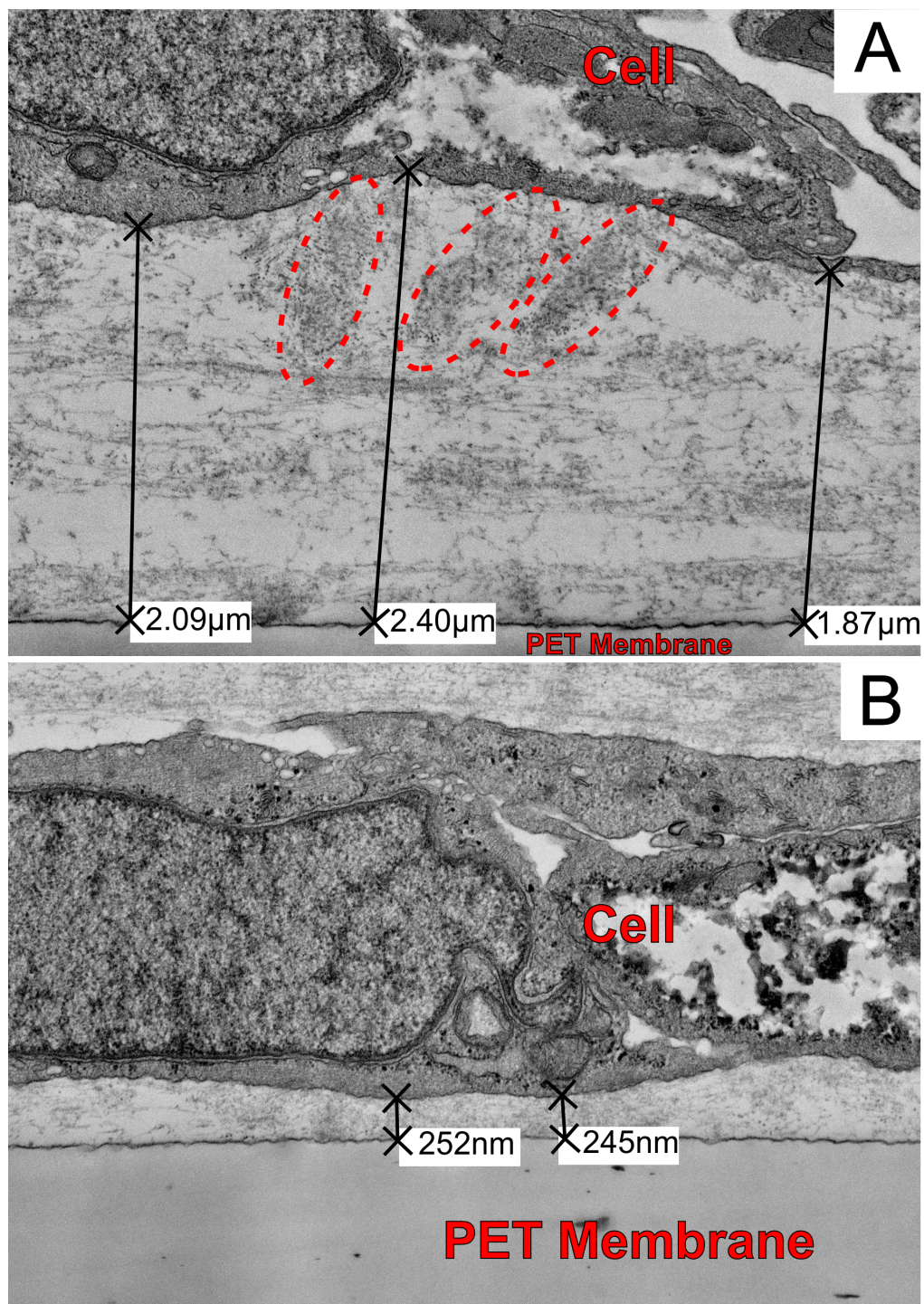


Fig. 3.6: TEM image shows the distance, as labeled, between the ARPE-19 cell layer and the porous membrane when (A) deposits are present (*ellipses*: Condensed deposits) and when (B) no deposits are formed. The cell layer and porous membrane layer are labeled in each image.

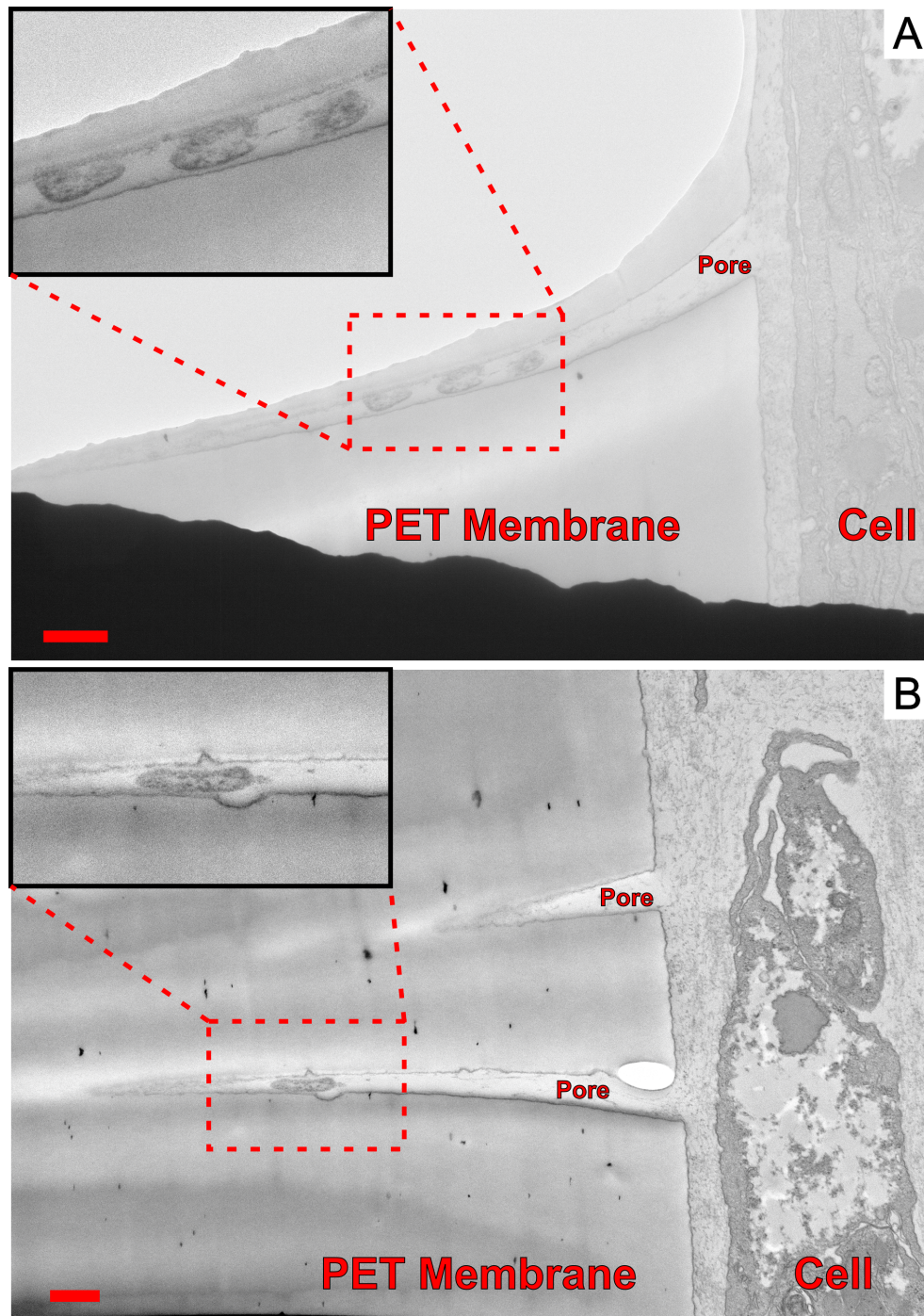


Fig. 3.7: TEM images showing examples of cellular debris deposits lodged in the channels of the $0.4\mu\text{m}$ pores of the porous membrane. (A) Shows a single pore with three membranous deposits lodged in the pore. (B) Shows two pores in the membrane with a membranous deposit in one of the pores. The insert in each image provides a zoomed-in view of the deposits for improved contrast. The PET membrane, cell layer, and pore openings are labeled in each image. (Scale bars, 500 nm in A and B.)

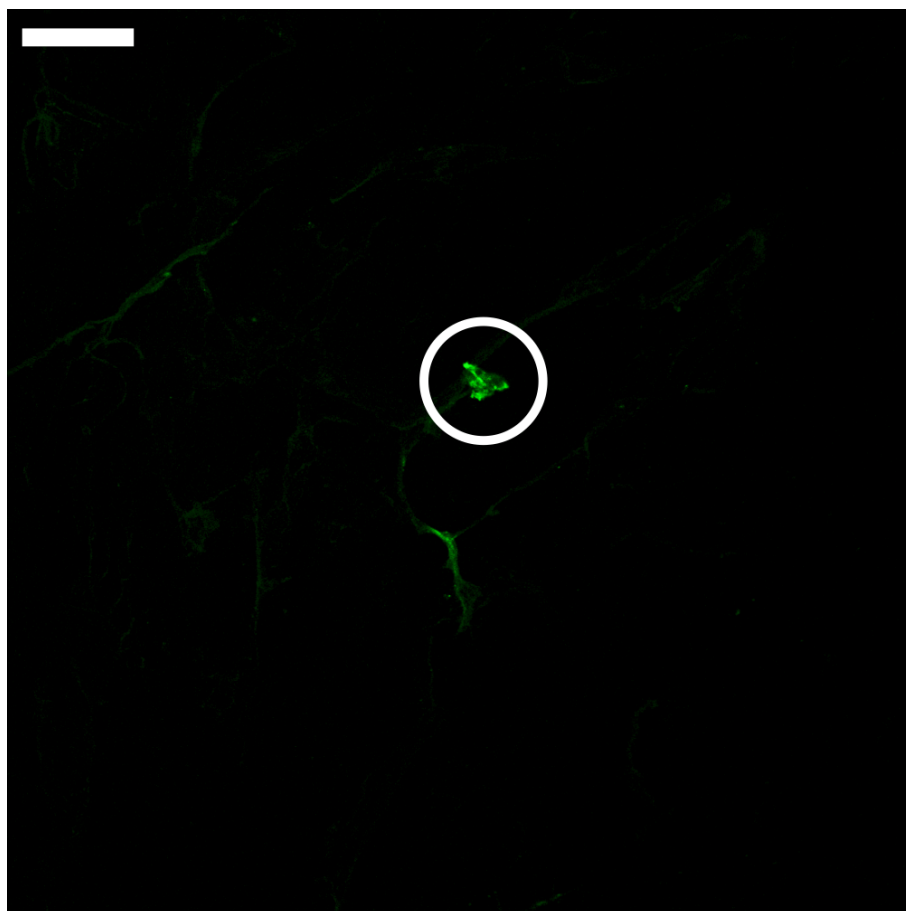


Fig. 3.8: Confocal microscopy image with ApoE staining of an ARPE-19 cell culture after the five-week incubation period and the cell layer has been removed using trypsin. The circle indicates the presence of a sub-RPE deposit on the porous membrane, even after the removal of the cell layer. (Scale bar, 50 μm .)

non-trypsinized, 5-Week samples. The reason for this may be that large deposits are able to better withstand treatment with trypsin because of increased volume.

3.2.3 Discussion

We describe an *in vitro* model for early AMD that mimics the development of sub-RPE drusen-like deposits. The model uses an immortalized cell line of non-primary retinal pigment epithelium cells, ARPE-19 [70]. ARPE-19 cells were grown for a minimum of five weeks on porous membrane inserts with 0.45 μm diameter pores. The presence of discrete sub-RPE accumulations was verified through TEM imaging. Confocal microscopy fluorescent staining showed that ApoE and cholesterol, two major components of drusen, comprise the deposits [36–38, 43, 76, 78, 81]. In positively identifying the presence of naturally occurring drusen components in the sub-RPE deposits, we extend upon the work of Amin et al. [71]. The identification of known drusen constituents in sub-RPE deposits formed in a culture of non-primary cells has not previously been shown, according to Johnson et al. [80]. This cell model therefore presents a novel, non-primary option to study new treatment strategies such as laser ablation targeted at drusen *in vitro*. In developing this model, our goal was to create an experimental system for investigations into the laser pulse-tissue interaction between femtosecond laser pulses and sub-RPE drusen-like deposits; previous attempts at laser treatment have used continuous wave lasers and been unsuccessful [52].

The cell culture samples were examined after a minimum five-week incubation period with confocal microscopy to assay for the presence of known drusen components and with TEM to determine deposit position and structure. The

5-Week samples were compared to samples stained with identical protocols, but only grown for three days. Several previous proteome and lipid drusen investigations have identified both ApoE and cholesterol as constituents of human retinal drusen [36–38]. The presence of ApoE in the deposits is similar to the findings of Johnson et al. [80], who also reported significant levels of positive fluorescence for ApoE staining in their cell model created with primary human RPE cells. Simultaneous staining for ApoE and cholesterol detected deposits that fluoresced on two channels, indicating the presence of both components in discrete accumulations. However, the positive dual staining was not ubiquitous. It is possible that not all of the three deposit structural types identified by TEM, contain both ApoE and cholesterol. Confocal microscopy does not provide information on the specific deposit structure, and we were therefore unable to discern which of the three structures observed under TEM contained one or both of the drusen components.

TEM images clearly identified three different types of sub-RPE deposit structures, all of which correspond to three of those reported by Amin et al. [71], and two of which were reported by Johnson et al. [80]. In areas where deposits were observed, the cell layer was lifted measurably higher off the porous membrane layer compared to regions lacking observable deposits. TEM observation of the 3-Day control sample found no deposits beneath the RPE cell layer.

Importantly, TEM images showed accumulations of cellular material within the pores of the porous membrane in close proximity to areas of deposit formation. This suggests that the pores collect cellular debris, effectively blocking the path for material shed by the cells to diffuse away from the basal surface. We hypothesize

that prior to pore blockage or deposit formation, the cells exude material that freely passes through the 0.45 μm pores in the membrane and diffuses into the media below the insert. Eventually, debris may accumulate, due to some spontaneous dysfunction in the process of phagocytosis or basal exudation, and become lodged under the cell layer or embedded in a pore, disrupting the flow of detritus away from the cells. As material continues to be shed it now accumulates into a discrete deposit under the confluent cell layer. Our finding that ApoE-containing deposits are still detected on the membrane after removal of the cell layer with trypsin supports this conjecture. Being anchored within the pore may allow some deposits to withstand enzymatic digestion.

After observing the phenomenon of deposits developing out of blocked pores in the cell culture sample, we propose that this is representative of the conditions in the retina that lead to drusen formation in AMD. One of the main functions of the RPE cells is the phagocytosis of photoreceptor outer segments (OS) [13, 14]. The RPE cells digest the OS and recycle material back to the retina [20, 21]. The waste matter from the degradation process diffuses across the blood-retina barrier (BRB) into capillaries and the larger circulatory system [20, 31]. The retina is isolated from the circulatory system to maintain an immune privilege, and the RPE makes up the outer layer of the BRB [9, 17, 43]. The exclusion limit of the BRB has been an area of interest for decades [82]. Recent investigations into the permeability of the BRB have found that gold nanoparticles on the order of 20 nm introduced to the bloodstream are able to pass through into the retina; however, larger 100 nm particles were unable to pass the barrier [83–85]. Therefore, if the size of shed debris

increases and eventually surpasses the permeability limit, somewhere between 20-100 nm, the cell material will be unable to diffuse out of the sub-RPE space into the circulatory system. Three known contributors to AMD that have been manipulated to reproduce the disease in experimental systems are oxidative stress, antioxidant deficiency, and lysosomal enzyme dysfunction [19]. All three of these hallmarks of AMD have recently been shown to induce stress on the endoplasmic reticulum (ER) of the RPE, which will induce cell apoptosis after prolonged periods [19, 22, 30, 86]. Okubo et al. [19] injected a lysosomal inhibitor into rats that induced the formation of lipofuscin-like RPE accumulations. These accumulations are the result of inhibition of the RPE cells to metabolize the lipids from OS phagosomes. The lysosomes that merge with the phagosomes to break down the OS components contain lysosomal enzymes that are sensitive to pH levels [19–21]. A known component of lipofuscin, A2E, elevates lysosomal pH levels, inhibiting enzyme function and leading to ER stress [19]. Another cause of AMD that has been shown to stimulate ER stress is oxidative stress [30, 86]. Although antioxidant levels are known to decrease with age [87], other environmental factors such as cigarette smoke can also induce oxidative stress in the retina [30, 86]. Oxidative stress induces the inflammatory response and oxidizes lipoproteins, which hinder the degradation of lipids within RPE, leading to ER stress [22, 30, 88]. The result of stress on the ER of RPE cells is a reduction in the catabolism performance of these cells, leading to lipid droplet formation and accumulation of residual bodies within the cells [19–22]. The improperly degraded material accumulates within the BrM causing it to thicken, which, in conjunction with the larger size of cellular debris due

to reduced catabolism, makes lipid diffusion across the BRB more difficult [20, 21]. Thus, the improperly degraded cell material is stuck under the retina, as it is unable to pass through the pores of the thickened BRB. We propose a drusen development model in which as the RPE ages, the size of debris released from the cell after phagocytosis increases due to diminishing efficiency and functionality of the RPE cells. These large pieces of debris accumulate in the sub-RPE space to form drusen. Just as the pores in the porous membrane became blocked and sub-cellular deposits formed in our cell culture model, once the RPE phagocytosis process loses efficiency with age, larger pieces of cell debris cannot diffuse across the BRB and as a result accumulate into drusen. We believe the decline in phagocytosis performance of RPE cells is a contributing factor in the development of drusen in the sub-RPE space.

In conclusion, we developed an *in vitro* cell model using non-primary, ARPE-19 cells that develops drusen-like sub-RPE deposits, mimicking aspects of early AMD. This simple and readily reproducible system allows for the development of sub-cellular deposits with a composition similar to naturally occurring drusen. The method opens a new, more readily accessible avenue towards investigation into new treatments targeted at the early stages of AMD.

Chapter 4

Isolated femtosecond laser pulse ablation of sub-RPE drusen-like deposits

4.1 Motivation

With the confirmation of the cell culture model described in Chapter 3 developing sub-RPE drusen-like deposits, there is now a vehicle with which to explore novel laser-assisted treatment methods for age-related macular degeneration. As mentioned in Chapter 1, AMD is a progressive, degenerative condition that can lead to complete vision loss [10, 29]. While late stage AMD does present the more serious risk for patient vision loss, the progressive nature of the disease would suggest that the maximum therapeutic benefit would be achieved in halting the advancement in the earliest stages. And yet, current treatment strategies for AMD are aimed almost exclusively at late stage AMD. Only 10-15% of cases of AMD are categorized as late stage, therefore there are almost no methods to treat 85-90% of individuals with AMD [10, 29]. The only treatment protocol currently targeted at

early AMD is a proprietary blend of antioxidants supplements known as the AREDS formulation. This supplement formula was investigated in two clinical trials stages from 1992-2001 and 2006-2012, known as AREDS and AREDS2 respectively [40, 41]. However, administration of the AREDS formulation only produced statistically significant reduction in progression rates in individuals suffering from intermediate AMD in both eyes or advanced AMD in one eye [41]. For these groups, a 25% reduction in the risk of progression to late stage AMD was seen over a 5-year follow up window. Although the AREDS2 formulation is purportedly the only currently available treatment for AMD targeting the disease in the earliest stages, patients in the early stages saw no benefit [41, 42].

The treatment strategies that do exist are more accurately described as ways to manage symptoms or slow AMD as opposed to a cure that halts the progression of the disease entirely. Most contemporary AMD treatment strategies aim to curb the growth of neovascular blood vessels from the choroid, through holes in the RPE layer, into the retina; what is also known as wet late stage AMD or choroidal neovascularization. The current gold standard of treatment is routine intraocular injections of anti-vascular endothelial growth factor (anti-VEGF) [10, 17, 29, 43, 45]. A variety of laser assisted treatment strategies have previously been investigated; however, they have largely since been abandoned as the therapeutic benefit did not surpass the collateral damage [46–50, 89]. Approximately 8.7% of the world's population currently suffers from AMD, and that margin is expected to increase dramatically in the coming years as the global average age increases [42]. The monetary burden on global health care systems alone is anticipated to reach

\$255 billion [42], let alone the cost when patient quality of life is taken into consideration. The motivation, and obligation, to find an effective treatment for early stages of AMD is momentous.

4.1.1 Laser treatments for AMD

As discussed in depth in Chapter 1, a variety of different types of treatment for AMD have involved laser assistance. This includes photocoagulation or photodynamic therapy intended to cauterize choroidal neovascular blood vessels. As well as non-specifically targeted photocoagulation attempts to induce drusen resorption. The therapeutic benefits did not out-weigh the collateral damage induced by the thermal energy deposition of the continuous laser beams. All previous attempts at laser-assisted treatment were highly non-specific to the destructive AMD-induced material. Furthermore, the high levels of collateral healthy tissue damage caused side effects that over-shadowed the treatment potential of these methods.

4.1.2 Purpose of this study

This chapter explores the capabilities of femtosecond laser pulses when interacting with drusen-like deposits. The motivation of this entire thesis project was to obtain preliminary results demonstrating femtosecond laser pulses precisely and exclusively ablating sub-RPE drusen-like deposits. It was important that the laser pulse-tissue interaction exclude the RPE cells, only exerting ablative power in the sub-RPE space, specifically upon the drusen. Successful sub-RPE deposit ablation was achieved with an appropriately selected laser power and exposure window. To

date, this is the first demonstration of fs laser ablation of drusen-like deposits in an *in vitro* model, and may have implications for the treatment of dry AMD.

Femtosecond laser pulse-tissue interaction has been investigated extensively for a variety of biological applications. Ultrafast lasers have been demonstrated as a tool for intra-tissue nano-dissection of single plastids [90], dissection of fixed and dried metaphase human chromosomes [91], and the ablation of a single mitochondrion [92]. Additionally, fs laser-pulses have been used to non-invasively create reversible pores on the membranes of live cells and zebrafish embryos [61, 64, 93, 65]. This work was motivated in part to demonstrate the superior isolated ablative power of the femtosecond laser pulses compared to longer, non-ultrafast laser pulses. Guymer et al. [62] reported drusen area reduction in eyes treated with a 3 ns pulse. They claim the therapeutic benefits are due to a non-thermal rejuvenating process within the RPE cells that the laser stimulates, not leaving any scar, lesion, or collateral damage. However, it has been reported many times that RPE cells are post-mitotic and do not proliferate or possess strong wound repair capabilities in older individuals [23, 24]. Additionally, after claiming the results are from a non-thermal nanosecond process, they elaborate that the effects are due to steam vapor formation around intracellular organelles [62]. Thus, they claim they are not inducing thermal energy damage but only because they are demonstrating a thermo-mechanical injury. The assumption we seek to prove is that if positive therapeutic effects were observed when a nanosecond laser pulse was administered, the therapeutic benefits will be greatly improved upon in using a femtosecond laser pulse.

4.2 Femtosecond laser pulse ablation of sub-RPE deposits

4.2.1 Experimental Methodology

The ARPE-19 cell culture model outlined in Chapter 3 was used in this investigation. For laser application the porous membrane, on which the cells were seeded and incubated, was excised from the plastic insert and placed in a glass dish with 5 ml of PBS.

4.2.1.1 Fluorescence imaging and laser delivery setup

The fluorescence imaging system and optical setup used were those of Kohli et al. [65] and Katchinskiy et al. [94]. Briefly, the ApoE and filipin stains were observed with standard Endow GFP Longpass (Chroma Technology, En GFP LP 41018) and Quantum Dot 605 (Chroma Technology, Qdot) filters, respectively, mounted in a modified upright Nikon Eclipse 80i microscope. Fluorescence images were captured using the 10 megapixel Amscope MU1003 camera and with the Amscope imaging software. A 60x microscope objective with numerical aperture of 1.0 was used to enable imaging of the cell sample, focusing the laser beam to an approximate spot size of 800 nm. The laser was a titanium sapphire laser oscillator delivering 10 fs pulses at a repetition rate of 80 MHz with a center wavelength of 800 nm; the pulse energy was varied between 1.9-4.2 nJ/pulse. The exposure time was regulated by a computer-controlled, galvanometer-mounted mirror, programmed to expose the sample to the laser beam in windows of 15 ms pulse trains. The total

exposure time and pulse energy were varied to determine the optimal ablation parameters, which were evaluated through visual observation of deposit removal.

4.2.2 Results

Drusen-like sub-RPE deposits in the cell culture model were targeted for ablation with pulse trains from the fs laser while the overlying ARPE cells were left untouched. Figure 4.1 is a representation of the ultrafast laser pulse-tissue interaction during the cell culture model drusen-like deposit ablation process. The number of beam exposure windows required for complete deposit ablation varied based on the size of the deposit; therefore, the total pulse train dwell time for deposit removal was different for each deposit. The power level of the laser was also varied to optimize the ablation of the sub-RPE deposit while preserving the overlying RPE cell layer. To determine the parameters that induced substantial collateral damage to ARPE-19 cells, the laser beam was applied to ARPE-19 cells on glass plates to find the threshold point at which the laser damages the cells. The optimal window of operation for the femtosecond laser pulse during interaction with RPE cells was calibrated through variation of both the average power and length of pulse train delivery window. An average power level was chosen to be just above the level at which any interaction between the cells and laser beam becomes possible. In this case, below 0.875 nJ per pulse no interaction would occur between the cells and laser, regardless of dwell time, therefore 1 nJ per pulse was chosen as the average power level for this calibration investigation. The galvanometer-mounted mirror shutter speed was set to four different lengths: 1000ms, 500ms, 250ms, and 25ms. For multiple cells at each pulse train window setting, the number of pulse train

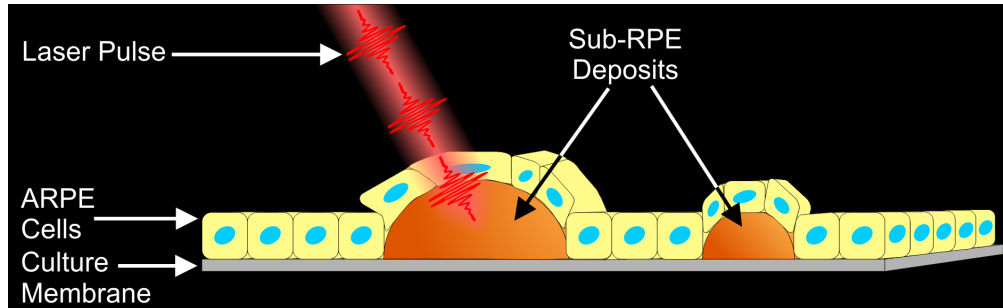


Fig. 4.1: Representation of the laser pulse-tissue interaction between the femtosecond laser pulses and sub-RPE drusen-like deposits. The femtosecond pulse trains pass harmlessly through the ARPE. The threshold leading to plasma-induced ablation is only surpassed at the point of focus of the laser, herein located on the drusen-like accumulation.

windows needed to induce three different visual stages of laser pulse-tissue interaction was recorded. The three stages of laser-tissue interaction were evaluated qualitatively and included the first visual interaction between cell and laser pulses (Fig. 4.2(B)), the point at which a lasting cavitation bubble is produced (Fig. 4.2(C)), and the point at which the cell membrane begins to leak (Fig. 4.2(D)). The average number of pulse train exposure windows needed to achieve each visual marker for the four varied exposure window lengths were plotted for comparison. The three longer pulse train window lengths had very similar trends, visual interaction and cavitation bubble formation happened with only a relative few pulse train exposures. To provide more control, a larger safe treatment zone, and a buffer against the negative cavitation bubble effects, the optimal experimental laser parameters were decided to be energy per pulse on the order of 1 nJ and a pulse train exposure window on the order of 25 ms.

In unsuccessful femtosecond laser pulse ablation attempts visible scars were left on the overlying cell layer after laser application. Figure 4.3 depicts the conditions before and after laser application with laser pulse parameters that exceeded the range capable of focusing through to the sub-RPE deposit without affecting the cell layer. The energy per laser pulse in this case was 4.2 nJ and the total beam dwell time was 1.3 s. The damage to the cell layer from the laser application with non-optimized focusing and power parameters is evident from the dark shadow (Fig. 4.3(B)). This artifact indicates a region of the cell that has been ablated along with the deposit material ablated below the cell layer. After the laser exposure the deposit accumulation is visibly disrupted as seen in Fig. 4.3(D).

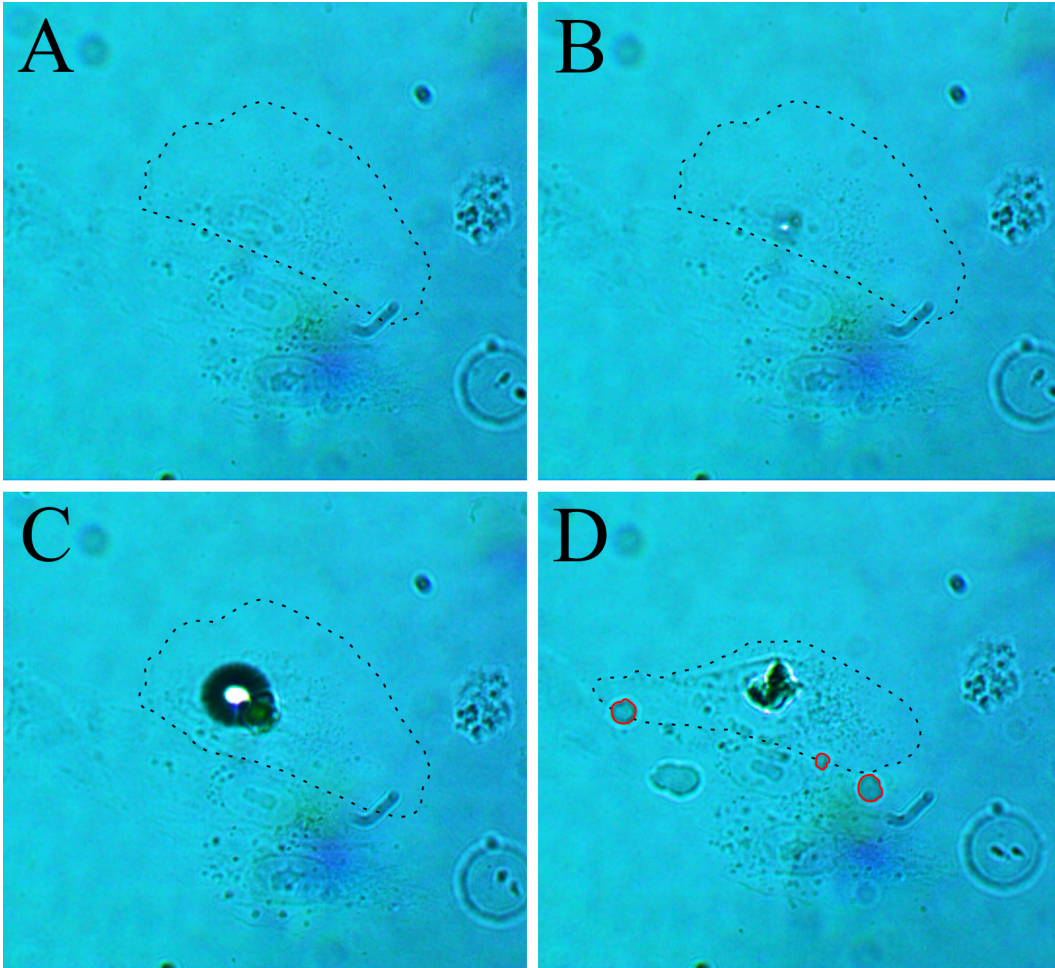


Fig. 4.2: Image captured through a microscope at 60x of an ARPE19 cell in the various categorical stages of interaction with the laser pulses during investigation into ablation parameters. (A) shows the cell upon initial inspection, prior to any laser pulse exposure. In (B), the first visual evidence of femtosecond pulse interaction with the cell is visible. A large, lasting cavitation bubble induced by pulse exposure windows is seen in (C). In (D), the cell has been significantly deformed and areas of fluid leakage from the cell are highlighted by a red outline. The cell outline is highlighted by a black dotted line in each image.

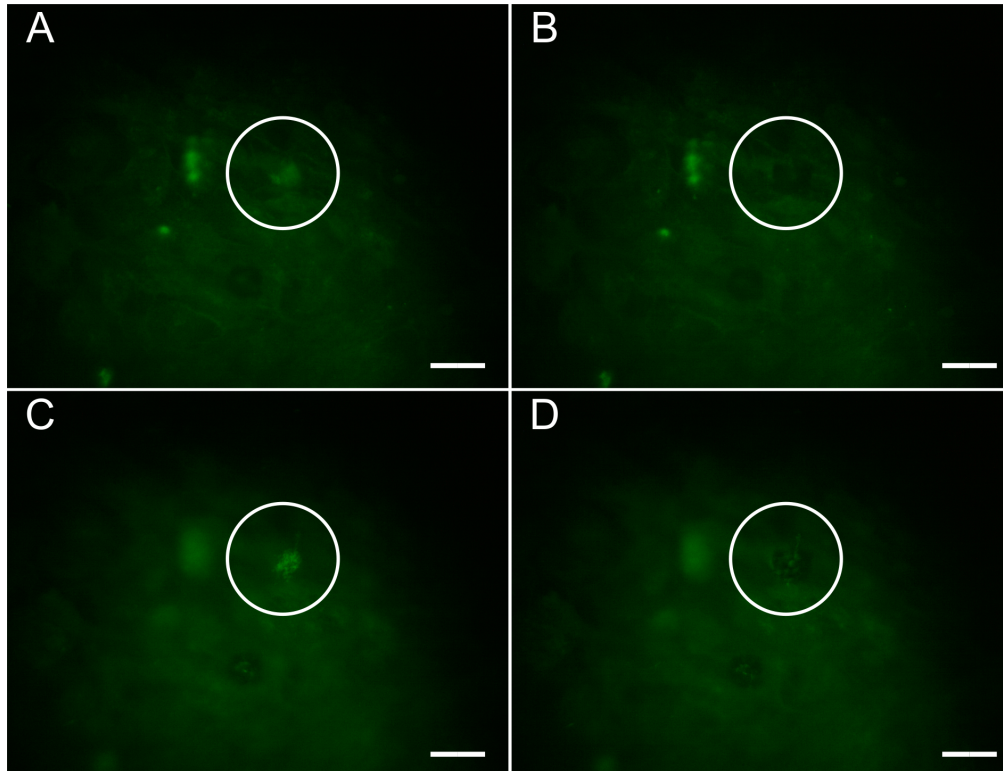


Fig. 4.3: Fluorescence microscopy image, stained for ApoE, of a sub-RPE deposit before and after unsuccessful laser ablation. The plane of focus was on the ARPE-19 cell layer in (A) and (B) and was below the cells on a sub-RPE deposit in (C) and (D). (A) and (C) were taken before the laser pulse exposure and (B) and (D) were taken after the laser delivery. (A) shows the fluorescent signal of the deposit visible through the cell layer. (B) highlights the shadow of scarring caused by damage to the cell layer during laser delivery to the sub-cellular space. (C) shows the deposit before laser ablation. (D) demonstrates the absence of the deposit after laser pulse delivery. The white circle highlights the same area of interest in each image. (Scale bars, 10 μm in A-D.)

The trials of laser ablation seen in Fig. 4.3 were successively improved upon during many attempts, until laser parameters that led to isolated and reproducible sub-RPE deposit removal without collateral cellular damage were determined. A successful sub-RPE deposit ablation is shown in Figure 4.4. In Fig. 4.4(A), as in Fig. 4.3(A), the signal from the sub-RPE deposit is visible through the cell layer when the microscope focal plane is on the cell layer. After laser exposure, the deposit signal is no longer visible through the cells and the cell layer remains untouched, with no observable shadow or artifact to indicate damage to the cells (Fig. 4.4(B)). The sub-RPE deposit targeted for ablation (Fig. 4.4(C)) is absent after the total beam exposure time of 150 ms at energy per pulse of 4.1 nJ (Fig. 4.4(D)).

Next, an experiment was performed to show that the deposits were ablated by the laser and not removed due to photobleaching of the fluorescent dye. Figure 4.5 shows the laser ablation of a sub-RPE deposit that was identified by its protein and lipid composition with ApoE antibodies and filipin, respectively. ApoE lipoproteins and cholesterol are widely accepted to be two significant components of natural drusen [36–38]. Both stains were used so as to verify simultaneous lipid and protein composition in the sub-RPE deposits, mimicking the characteristics of *in vivo* drusen. ApoE antibodies provided good contrast and resolution while filipin allowed real time addition of more stain to investigate the presence of photobleaching. The deposit in Fig. 4.5 was ablated with energy per femtosecond pulse of 1.9 nJ and a total exposure time of 1.2 s. After the laser ablation, more filipin stain was pipetted into the dish to restore fluorescence to photobleached regions. A vertical and horizontal lines transect the deposit area, as indicated on

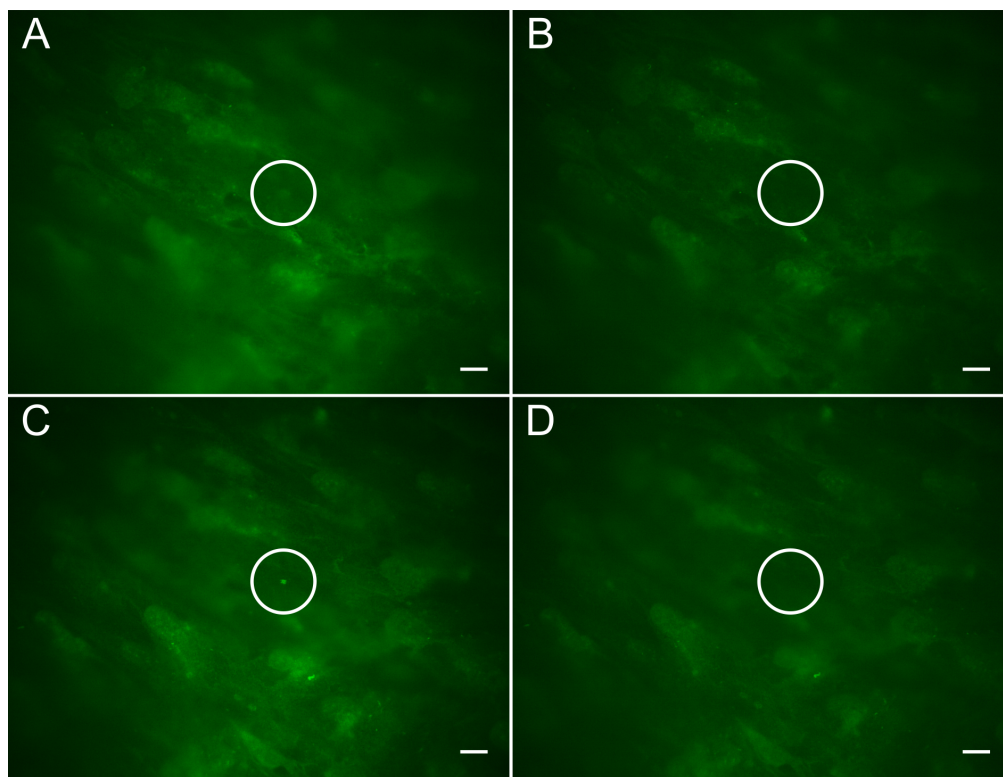


Fig. 4.4: Fluorescence microscopy, using ApoE staining, before and after the successful laser ablation of a sub-RPE drusen-like deposit. The focal plane was on the ARPE-19 cell layer in (A) and (B) and was below the cells on a sub-RPE deposit in (C) and (D). (A) and (C) were taken before the laser pulse exposure and (B) and (D) were taken after the laser delivery. In (A), the fluorescence of the sub-cellular deposit, shown in (C), can be seen through the cell layer. In both (B) and (D), the deposit is no longer visible and there is no damage or scarring to the cell layer as shown in (B). The white circle in each image highlights the same area of interest. (Scale bars, 20 μm in A-D.)

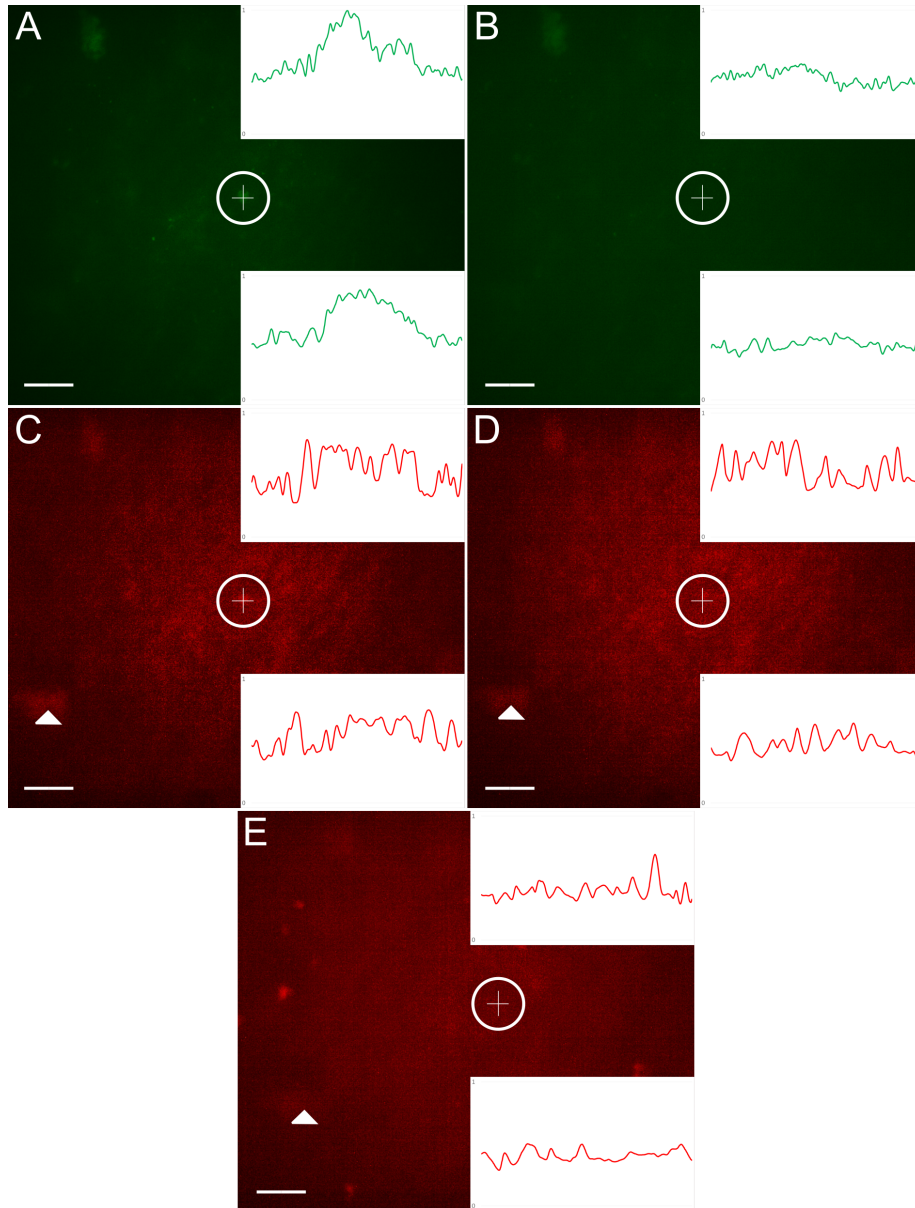


Fig. 4.5: Fluorescence microscopy image of a sub-RPE deposit, stained simultaneously for ApoE and cholesterol, before and after laser ablation. The ApoE channel is shown before (*A*) and after (*B*) laser ablation. The filipin channel is shown before (*C*) and after (*D*) laser ablation. The two inserts in each image show the normalized plots of pixel intensities along the vertical (top right) and horizontal (bottom right) lines seen in each frame. Before laser ablation, in (*A*) and (*C*), the line intensity plot shows the profile of the sub-RPE deposit. After laser ablation, the deposit contour has been destroyed, see (*B*) and (*D*). More filipin stain was added after (*D*) was taken. (*E*) is after 80 minutes had passed, areas within the image begin to regain fluorescence, but the deposit area pixel intensity does not return. The white circle in each image highlights the same region of interest. The white arrowheads in (*C*)-(*E*) label a fluorescent deposit used as a landmark during the image acquisition. (Scale bars, 20 μm in *A*-*E*.)

each image, and were displayed as a graph of normalized pixel intensity values along that line. In Fig 4.5(A), the profile of the deposit is easily identified in the two line intensity plots. Comparing these plots to those found in Fig. 4.5(B) highlights the removal of the deposit material, as the deposit profile is no longer present. The line intensity plots in Fig. 4.5(C)-(E) are not as revelatory due to the amount of noise from the poor contrast and excessive background fluorescence of these images. It can be clearly seen in Fig. 4.5(E) that with additional filipin some accumulations in the frame regained their fluorescent signal. In contrast to these freshly fluorescent spots, the region within the white circle, where the deposit had been before the laser application, remained dark.

To show that filipin stained deposits, photobleached from excitation source exposure, will regain their fluorescence signal, the same experiment was performed on a sample without laser pulse exposure. Figure 4.6 shows the results of leaving the sample under the excitation source for an extended period until the signal had been significantly reduced, adding more filipin stain to the dish, and waiting 60 minutes after adding the stain. The sample was left under the open excitation shutter for several minutes until the fluorescence was severely bleached (Fig. 4.6(B)). At that point, more filipin was added to the dish and left for 60 minutes. Some areas of fluorescence did return to the sample.

4.2.3 Discussion

The non-linear multiphoton absorption from exposure to focused fs laser pulses causes the excitation of electrons to the point of plasma-mediated ablation [1, 57]. The fs laser pulses create high-density plasmas in the targeted material after

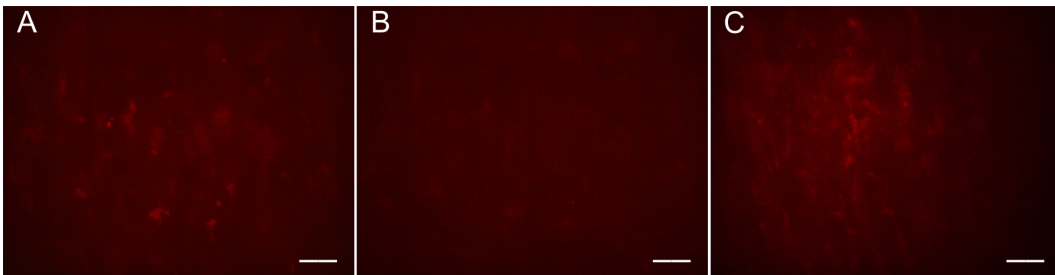


Fig. 4.6: Filipin fluorescence microscopy of an ARPE-19 sample with sub-RPE deposits. (A) was taken immediately after the excitation shutter was opened, showing the baseline fluorescence for the sample. (B) shows the photobleached sample after prolonged and continual excitation source exposure. More filipin stain was added to the dish after (B) was taken. (C) was taken 60 minutes after the addition of more filipin and shows that some cholesterol rich deposits regain their fluorescence after photobleaching if more filipin is added. (Scale bars, 20 μm in A-C.)

exceeding the power density threshold. This makes fs laser pulses an excellent tool for tissue manipulation as the effects of the laser pulse-tissue interaction are highly confined to the point of focus and induced plasma.

In this study, we targeted sub-RPE drusen-like deposits in a cell culture model, with fs laser pulses to demonstrate the ability to remove the sub-RPE deposits while the overlying cell layer was left unharmed. The laser parameters used in this method are crucial to the success of the ablation. The non-linear multiphoton absorption and electron excitation processes that lead to plasma formation are unique to ultrafast fs laser pulses [1, 57, 65]. There is no collateral damage to cells or tissue outside of the point of focus of the laser when fs laser pulses are applied.

The important laser parameters included the average power level and the beam exposure time. As seen in Fig. 4.3, a combination of high power level and long exposure time will lead to visible damage to the cells overlying the targeted deposit. The damage caused by the incorrect laser parameters used in this case is easily seen when comparing the area before and after laser application. Thus, optimal ablation parameters are essential to prevent damage to cells surrounding the sub-RPE deposits during successful, isolated ablative removal. Figure 4.4 presents one example of a sub-RPE deposit ablation without collateral damage to the cell layer above the deposit or any of the tissue surrounding the targeted deposit. The laser point of focus was able to penetrate the cell layer and interact only with the sub-RPE deposit. The laser tissue interaction was also confined within the diffraction limited spot size of the laser beam, as no tissue damage is visible anywhere outside of where the laser pulses were applied.

The successful deposit ablation experiment shown in Figure 4.4 is the first example of ultrafast laser ablation of sub-RPE drusen-like deposits in a cell culture model. A vitality test on the ARPE-19 cells after the laser ablation procedure was not performed; thus, preservation of the cell layer after laser ablation of an underlying sub-RPE deposit was verified by qualitative visual investigation of the cell morphology. The ARPE-19 cells used in this experiment are non-pigmented, unlike *in vivo* RPE cells, which contain melanosomes [10, 13, 29]. The pigmentation of the overlying epithelium cells would not affect the absence of collateral damage during the plasma-mediated ablation of drusen. The laser intensity during the ablation is low enough such that the cells outside of the focal point of the laser cannot undergo the non-linear multiphoton absorption required to initiate the ionization process. Additionally, the absorption spectrum of melanin displays negligible absorption of only 1% at 800 nm (percent absorption calculation can be found in Appendix B), the wavelength we use in our investigation [95–97]. Therefore, the wavelength and time-scale of the laser used herein both eliminate the possibility of melanin presence in the RPE layer inducing laser-tissue interaction in these cells.

We verified that the disappearance of the drusen-like deposit was from laser ablation and not the photobleaching of the fluorophores used to identify the deposits. The removal of the deposit in Fig. 4.5 after the laser ablation is much more easily observed in the ApoE channel (Fig. 4.5(A)-(B)) over the filipin channel (Fig. 4.5(C)-(D)). However, the filipin images are important in the verification of true ablation as opposed to photobleaching. The removal of the deposit from the field of

view after the laser application was indeed due to the laser-induced destruction of the material rather than the photobleaching of the fluorophores within the deposit.

The visibility of the deposit removal is more difficult to observe in the channel with the filipin stain when compared to the ApoE channel. The normalized line intensity graphs inset into each image of Fig. 4.5 seek to help highlight the removal of the deposit. There is an observable change in the intensity profile in the filipin channel before and after laser ablation. However, the inherent noise in these images makes a definitive confirmation that the deposit seen before the ablation was fully destroyed after the laser exposure difficult. Figure 4.5(E) represents a threshold of the noise in the image given that this image was taken well after the ablation occurred when there was no remaining deposit material observable in the highlighted area of interest. Thus, the normalized pixel values in the plot here are almost exclusively from background fluorescence noise. The sample in Fig. 4.6 did not undergo laser ablation, but was photobleached through excitation exposure. This set of images is proof that after photobleaching, adding more filipin will restore visibility of remaining sub-RPE deposits. Thus, when the drusen-like deposit does not return in Fig. 4.5(E), after addition of filipin and time for the stain to react, the conclusion can be drawn that the deposit removal is from the ablative power of the laser, not from the effects of photobleaching. The quality of the images, specifically the contrast levels, in the filipin channel is significantly reduced compared to the ApoE channel. But the ApoE antibody staining protocol did not permit re-staining while the sample was in the optical setup; thus, photobleaching investigations had to be done with filipin. This image quality discrepancy can potentially be attributed to

a variety of reasons including the increased specificity of the ApoE stain. The filipin stain is diffuse throughout the sample, including the background, thus reducing the contrast of the image. Additionally, filipin photobleaches quite rapidly, making capturing images of comparable quality to the protein stain difficult.

Herein, we demonstrate that sub-RPE drusen-like deposits can be removed using pulses from an ultrafast femtosecond laser. The laser pulses can be focused through the RPE cell layer and remove the underlying deposit material while leaving the healthy RPE cells undamaged.

The technique we have demonstrated is the first time femtosecond laser pulses were used for the targeted laser ablation of sub-RPE deposits that mimic those seen in AMD. Currently, there is no cure for AMD, only methods for managing the complications of disease progression. We suggest that this laser surgery technique for removing drusen deposits while preserving the remaining healthy RPE cells may halt or slow the progression of this degenerative disease. With further research into this new treatment, the millions of patients affected by AMD can potentially be spared from the vision loss caused by the progression of AMD.

Chapter 5

Conclusion and future prospects

5.1 Conclusion and future prospects

Age-related macular degeneration is a serious condition that progressively deteriorates the sharp, focused, central visual field. This disease is the leading cause of blindness in the developed world, affecting millions of people across the globe [5]. The prevalence and impact of AMD is only expected to increase in coming years as the mean age of the global population continues to increase. Most pressing is that this widespread condition does not have a cure.

At present, all forms of treatment for AMD either attempt to slow the progression of the disease, without fully stopping it, or alleviate the symptoms as they arise, without treating the root cause. As discussed in depth in Chapter 1 and 4, most attempts at treatment for AMD target the latest stages of the progressive disease, when a substantial amount of damage to the retina has already occurred. Additionally, only a fraction of all cases of AMD are categorized as advanced and capable of receiving treatments, meaning nearly 90% of all those with AMD have no options [10].

Ultrafast lasers, specifically femtosecond lasers, are of keen interest in the continued exploration of treatment for AMD because of the unique femtosecond laser pulse-tissue interaction that occurs on this time scale. The spatial resolution of femtosecond laser pulses, the ability to only induce laser ablation at only the focal point of the beam, is very important in enabling the isolated ablation of deposits underneath the retina and RPE layer, without further damaging those important cellular structures. Characteristic of femtosecond laser pulse-tissue interaction is no thermal damage from the laser-assisted treatment, potentially eliminating negative side effects of retinal laser treatment and maximizing therapeutic benefits.

Within this work are discussed several different measures in the search for preliminary results demonstrating the capability of femtosecond laser pulses to precisely ablate drusen deposits associated with AMD. A prototype of a clinical treatment device is described in Chapter 2. Chapter 3 sees the development of an acceptable experimental model for drusen-like sub-RPE deposits, which is then used in Chapter 4 when the isolated femtosecond ablation is demonstrated. The work done in Chapter 4 demonstrating the successful ablation of a sub-RPE deposit would not have been possible without the work described in Chapter 3 to create a suitable sample for experimentation. As a whole this work represents but the first, albeit important, preliminary step in advancing femtosecond laser systems as a clinical tool for the treatment of AMD during the earliest stages of the disease.

5.1.1 Histological and viability assay

Creating the ARPE-19 cell culture model and demonstrating the isolated ablation of sub-RPE deposits is but the first step in a very long journey to obtain

permission for this technology to be used as a clinical tool. Now that positive preliminary results have been collected using a non-primary cell culture model, the next step would be to repeat the experiments using a primary cell line, or better yet, using donor tissue enucleated from individuals with AMD. Using the preliminary ablation results from this work, a successful application was made to the donor tissue bank in order to gain access to enucleated human eyes with AMD present. This means the next step of investigations can be made on primary cells exhibiting AMD symptoms, making the experimental system, and therefore the conclusions drawn, one step closer to the situation observed *in vivo*.

A component in the next step of this process that will be of paramount importance is to perform tests on the RPE cells post laser ablation. A histological assay on two slices from a single retinal sample, one that is and one that is not laser ablated, would show not only what specific proteins and lipids are present in a particular sample, but also how the femtosecond laser ablation process might denture or change the proteins found in the drusen. Additionally, a vitality assay on the RPE cells would also be a big step for this research. The ablation assay described in this work relied on qualitative evaluation of the RPE cells post-ablation to determine if significant trauma had been done to the cells. In the next step, performing a vitality assay on the RPE cells after administering the laser would quantitatively prove whether the femtosecond laser pulse is inducing any collateral damage upon surrounding tissue during the process of drusen ablation.

5.1.2 Future prospects

Overall this work has many implications and newly available avenues for future work. Two points that are typically deterrents from new research in the area of laser-assisted drusen ablation are solved with this work. The most significant being the creation of a cell culture model that develops drusen-like deposits using an immortalized cell line, meaning it is easier and more affordable for researchers new to the area of interest. Many different new investigations into treatments for AMD can be pursued using the ARPE-19 cell culture model. Additionally, many in ophthalmology believe lasers to be an inferior method of treatment because of the significant levels of collateral damage seen in previous treatment modalities. This project can introduce many new researchers to the capabilities, and in turn significant possibilities, of femtosecond laser assisted medicine.

Another future prospect for this work is to improve upon the initial slit lamp laser delivery prototype. Creating a clinical tool to be used in the treatment and eradication of AMD will require many more iterations of and improvements on the system described in Chapter 2. Maximizing safety features on the laser delivery device will be required prior to any sort of clinical testing. A suggestion for the next step on this prototype would be to automate the control system versus the manual control system currently in place. A computer would be much more precise and accurate in identifying drusen to be ablated, ablating said target drusen, and avoiding exclusion areas, such as the optic nerve head, in the process.

The vision for this research is to create a functional clinical tool that is being used by medical professionals to improve the lives of those living with this

debilitating disease. The results presented herein are a preliminary first step on an important and lengthy process of clinical approval.

References

1. Niemz MH (2002) *Laser-Tissue Interactions: Fundamentals and Applications*, 2nd ed. Springer-Verlag, Berlin, Heidelberg.
2. Matthias B, Zabic M, Brockmann D, et al (2016) Adaptive optics assisted and optical coherence tomography guided fs-laser system for ophthalmic surgery in the posterior eye. *J Biomed Opt* 21:121512.
3. Boulais E, Lachaine R, Hatef A, Meunier M (2013) Plasmonics for pulsed-laser cell nanosurgery: Fundamentals and applications. *J Photochem Photobiol C Photochem Rev* 17:26–49.
4. Manenkov AA (2014) Fundamental mechanisms of laser-induced damage in optical materials: today's state of understanding and problems. *Opt Eng* 53:10901.
5. Congdon N, O'Colmain B, Klaver CCW, et al (2004) Causes and prevalence of visual impairment among adults in the United States. *Arch Ophthalmol* (Chicago, Ill 1960) 122:477–485.
6. Bourne RRA, Jonas JB, Flaxman SR, et al (2014) Prevalence and causes of vision loss in high-income countries and in Eastern and Central Europe: 1990-2010. *Br J Ophthalmol* 98:629–638.
7. Ding X, Patel M, Chan C-C (2009) Molecular pathology of age-related macular degeneration. *Prog Retin Eye Res* 28:1–18.
8. CNIB About AMD. <http://www.cnib.ca/en/your-eyes/eye-conditions/eye-connect/AMD/About/Pages/default.aspx>.

9. Kolb H (2012) Simple Anatomy of the Retina. In: Kolb H, Fernandez E, Nelson R, editors. *Webvision Organ Retin Vis Syst* [Internet] Salt Lake City (UT): University of Utah Health Sciences Center.
10. Holz FG, Pauleikhoff D, Spaide RF, Bird AC (2004) Holz FG, Pauleikhoff D, Spaide RF, Bird AC, editors. *Age-related macular degeneration*, 1st ed. Springer-Verlag, Berlin, Heidelberg.
11. Kolb H (2012) Gross Anatomy of the Eye. In: Kolb H, Fernandez E, Nelson R, editors. *Webvision Organ Retin Vis Syst* [Internet] Salt Lake City (UT): University of Utah Health Sciences Center.
12. Farag ES, Vinters HV, Bronstein J (2009) Pathologic findings in retinal pigment epithelial cell implantation for Parkinson disease. *Neurology* 73:1095–1102.
13. Strauss O (2011) The Retinal Pigment Epithelium. In: Kolb H, Fernandez E, Nelson R, editors. *Webvision Organ Retin Vis Syst* [Internet] Salt Lake City (UT): University of Utah Health Sciences Center.
14. Mazzoni F, Safa H, Finnemann SC (2014) Understanding photoreceptor outer segment phagocytosis: Use and utility of RPE cells in culture. *Exp Eye Res* 126:51–60.
15. Strauss O (2005) The Retinal Pigment Epithelium in Visual Function. *Physiol Rev* 85:845–881.
16. Nickla DL, Wallman J (2010) The Multifunctional Choroid. *Prog Retin Eye Res* 29:144–168.
17. Campbell M, Humphries P (2012) The blood-retina barrier: tight junctions

- and barrier modulation. *Adv Exp Med Biol* 763:70–84.
18. Curcio CA, Johnson M (2012) Structure, Function, and Pathology of Bruch's Membrane. In: *Retina*, 5th ed. Elsevier, pp 465–481.
 19. Okubo A, Sameshima M, Unoki K, et al (2000) Ultrastructural changes associated with accumulation of inclusion bodies in rat retinal pigment epithelium. *Invest Ophthalmol Vis Sci* 41:4305–4312.
 20. Bird AC (2010) Therapeutic targets in age-related macular disease. *J Clin Invest* 120:3033–3041.
 21. Holz FG, Pauleikhoff D, Klein R, Bird AC (2004) Pathogenesis of lesions in late age-related macular disease. *Am J Ophthalmol* 137:504–510.
 22. Salminen A, Kauppinen A (2010) Endoplasmic reticulum stress in age-related macular degeneration: trigger for neovascularization. *Mol Med* 16:535–542.
 23. Stern J, Temple S (2015) Retinal pigment epithelial cell proliferation. *Exp Biol Med* 240:1079–1086.
 24. Defoe DM, Adams LBS, Sun J, et al (2007) Defects in retinal pigment epithelium cell proliferation and retinal attachment in mutant mice with p27 Kip1 gene ablation. *Mol Vis* 13:273–286.
 25. Dorey CK, Wu G, Ebenstein D, et al (1989) Cell loss in the aging retina: Relationship to lipofuscin accumulation and macular degeneration. *Investig Ophthalmol Vis Sci* 30:1691–1699.
 26. Katz ML, Robison WG (2002) What is lipofuscin ? Defining characteristics and differentiation from other autofluorescent lysosomal storage bodies. *Arch Gerontol Geriatr* 34:169–184.

27. Krohne TU, Stratmann NK, Kopitz J, Holz FG (2010) Effects of lipid peroxidation products on lipofuscinogenesis and autophagy in human retinal pigment epithelial cells. *Exp Eye Res* 90:465–471.
28. Fletcher EL, Jobling AI, Vessey KA, et al (2011) Animal models of retinal disease. *Prog Mol Biol Transl Sci* 100:211–286.
29. Hageman GS, Gehrs K, Johnson LV, Anderson D (2008) Age-Related Macular Degeneration (AMD). In: Kolb H, Fernandez E, Nelson R, editors. *Webvision Organ Retin Vis Syst* [Internet] Salt Lake City (UT): University of Utah Health Sciences Center.
30. Kunchithapautham K, Atkinson C, Rohrer B (2014) Smoke exposure causes endoplasmic reticulum stress and lipid accumulation in retinal pigment epithelium through oxidative stress and complement activation. *J Biol Chem* 289:14534–14546.
31. Anderson DH, Mullins RF, Hageman GS, Johnson LV (2002) A role for local inflammation in the formation of drusen in the aging eye. *Am J Ophthalmol* 134:411–431.
32. Abdelsalam A, Del Priore L, Zarbin MA (1999) Drusen in age-related macular degeneration: pathogenesis, natural course, and laser photocoagulation induced-regression. *Surv Ophthalmol* 44:1–29.
33. Spaide RF, Curcio CA (2010) Drusen Characterization With Multimodal Imaging. *Retina* 30:1441–1454.
34. Curcio CA, Presley JB, Malek G, et al (2005) Esterified and unesterified cholesterol in drusen and basal deposits of eyes with age-related

- maculopathy. *Exp Eye Res* 81:731–741.
35. Johnson PT, Lewis GP, Talaga KC, et al (2003) Drusen-associated degeneration in the retina. *Investig Ophthalmol Vis Sci* 44:4481–4488.
 36. Wang L, Clark ME, Crossman DK, et al (2010) Abundant lipid and protein components of drusen. *PLoS One* 5:e10329.
 37. Haimovici R, Gantz DL, Rumelt S, et al (2001) The lipid composition of drusen, Bruch's membrane, and sclera by hot stage polarizing light microscopy. *Invest Ophthalmol Vis Sci* 42:1592–1599.
 38. Crabb JW, Miyagi M, Gu X, et al (2002) Drusen proteome analysis: an approach to the etiology of age-related macular degeneration. *Proc Natl Acad Sci USA* 99:14682–14687.
 39. Davis MD, Gangnon RE, Lee L-Y, et al (2005) The Age-Related Eye Disease Study severity scale for age-related macular degeneration: AREDS Report No. 17. *Arch Ophthalmol (Chicago, Ill 1960)* 123:1484–1498.
 40. Vitale S, Clemons TE, Agrón E, et al (2016) Evaluating the Validity of the Age-Related Eye Disease Study Grading Scale for Age-Related Macular Degeneration: AREDS2 Report 10. *JAMA Ophthalmol* 134:1041–1047.
 41. Age-Related Eye Disease Study Research Group (2001) A Randomized, Placebo-Controlled, Clinical Trial of High-Dose Supplementation With Vitamins C and E, Beta Carotene, and Zinc for Age-Related Macular Degeneration and Vision Loss: AREDS Report No. 8. *Arch Ophthalmol* 119:1417–1436.
 42. Hanus J, Zhao F, Wang S (2016) Current therapeutic developments in

- atrophic age-related macular degeneration. *Br J Ophthalmol* 100:122–127.
43. Shin OR, Kim YH (2013) Age-related macular degeneration (AMD): Current concepts in pathogenesis and prospects for treatment. *Tissue Eng Regen Med* 10:164–175.
 44. Bunting R, Guymer R (2012) Treatment of age-related macular degeneration. *Aust Prescr* 35:90–94.
 45. Gillies MC, Campain A, Barthelmes D, et al (2015) Long-Term Outcomes of Treatment of Neovascular Age-Related Macular Degeneration Data from an Observational Study. *Ophthalmology* 122:1837–1845.
 46. Kallitsis A, Moschos MM, Ladas ID (2007) Photodynamic Therapy versus Thermal Laser Photocoagulation for the Treatment of Recurrent Choroidal Neovascularization due to AMD. *In Vivo (Brooklyn)* 21:1049–1052.
 47. Kawczyk-Krupka A, Bugaj AM, Potempa M, et al (2015) Vascular-targeted photodynamic therapy in the treatment of neovascular age-related macular degeneration: Clinical perspectives. *Photodiagnosis Photodyn Ther* 12:161–75.
 48. Zhu L, Banerjee RK, Salloum M, et al (2008) Temperature distribution during ICG-dye-enhanced laser photocoagulation of feeder vessels in treatment of AMD-related choroidal neovascularization. *J Biomech Eng* 130:31010.
 49. Friberg TR, Musch DC, Lim JI, et al (2006) Prophylactic Treatment of Age-Related Macular Degeneration Report Number 1: 810-Nanometer Laser to Eyes with Drusen. Unilaterally Eligible Patients. *Ophthalmology* 113:612–

623.

50. Friberg TR, Brennen PM, Freeman WR, Musch DC (2009) Prophylactic Treatment of Age-Related Macular Degeneration Report Number 2: 810-Nanometer Laser to Eyes with Drusen: Bilaterally Eligible Patients. *Ophthalmic Surgery, Lasers & Imaging* 40:530–539.
51. Wood JPM, Plunkett M, Previn V, et al (2011) Nanosecond Pulse Lasers for Retinal Applications. *Lasers Surg Med* 43:499–510.
52. Virgili G, Michelessi M, Parodi MB, et al (2015) Laser treatment of drusen to prevent progression to advanced age-related macular degeneration. *Cochrane Database Syst Rev*.
53. Lavinsky D, Sramek C, Wang J, et al (2014) Subvisible retinal laser therapy: titration algorithm and tissue response. *Retina* 34:87–97.
54. Manevitch Z, Lewis A, Levy C, et al (2012) Subsurface Femtosecond Tissue Alteration: Selectively Photobleaching Macular Degeneration Pigments in Near Retinal Contact. *J Phys Chem B* 116:6945–6951.
55. Lim JI (2006) Hastening choroidal neovascularization: The irony of prophylactic laser in unilateral eyes with high-risk drusen. *Am J Ophthalmol* 141:354–355.
56. Guymer R (2002) Drug treatment of macular degeneration. *Aust Prescr* 25:116–119.
57. Bauerle D (2000) *Laser Processing and Chemistry*, 3rd ed. Springer-Verlag, Berlin, Heidelberg.
58. Boyd RW (1992) *Nonlinear Optics*, 1st ed. Academic Press, Inc., Boston.

59. Chen H, Liu J, Li H, et al (2015) Femtosecond laser ablation of dentin and enamel : relationship between laser fluence and ablation efficiency. *J Biomed Opt* 20:28004.
60. Vogel A, Noack J, Hüttman G, Paltauf G (2005) Mechanisms of femtosecond laser nanosurgery of cells and tissues. *Appl Phys B Lasers Opt* 81:1015–1047.
61. Kohli V, Robles V, Cancela ML, et al (2007) An alternative method for delivering exogenous material into developing zebrafish embryos. *Biotechnol Bioeng* 98:1230–1241.
62. Guymer RH, Brassington KH, Dimitrov P, et al (2014) Nanosecond-laser application in intermediate AMD: 12-month results of fundus appearance and macular function. *Clin Exp Ophthalmol* 42:466–479.
63. Brinkmann R, Huttmann G, Rogener J, et al (2000) Origin of Retinal Pigment Epithelium Cell Damage by Pulsed Laser Irradiance in the Nanosecond to Microsecond Time Regimen. *Lasers Surg Med* 27:451–464.
64. Kohli V, Elezzabi AY, Acker JP (2005) Cell nanosurgery using ultrashort (femtosecond) laser pulses: applications to membrane surgery and cell isolation. *Lasers Surg Med* 37:227–30.
65. Kohli V, Elezzabi AY (2008) Laser surgery of zebrafish (*Danio rerio*) embryos using femtosecond laser pulses: optimal parameters for exogenous material delivery, and the laser's effect on short- and long-term development. *BMC Biotechnol* 8:7.
66. Chidlow G, Shibebe O, Plunkett M, et al (2013) Glial cell and inflammatory

- responses to retinal laser treatment: Comparison of a conventional photocoagulator and a novel, 3-nanosecond pulse laser. *Investig Ophthalmol Vis Sci* 54:2319–2332.
67. Ramkumar HL, Zhang J, Chan CC (2010) Retinal ultrastructure of murine models of dry age-related macular degeneration (AMD). *Prog Retin Eye Res* 29:169–190.
 68. Ambati J, Anand A, Fernandez S, et al (2003) An animal model of age-related macular degeneration in senescent Ccl-2- or Ccr-2-deficient mice. *Nat Med* 9:1390–1397.
 69. Coffey PJ, Gias C, McDermott CJ, et al (2007) Complement factor H deficiency in aged mice causes retinal abnormalities and visual dysfunction. *Proc Natl Acad Sci USA* 104:16651–16656.
 70. Dunn KC, Aotaki-Keen AE, Putkey FR, Hjelmeland LM (1996) ARPE-19, a human retinal pigment epithelial cell line with differentiated properties. *Exp Eye Res* 62:155–169.
 71. Amin S, Chong NH, Bailey TA, et al (2004) Modulation of Sub-RPE deposits in vitro: a potential model for age-related macular degeneration. *Invest Ophthalmol Vis Sci* 45:1281–1288.
 72. Espiritu DJ, Huang ZH, Zhao Y, Mazzone T (2010) Hyperglycemia and advanced glycosylation end products suppress adipocyte apoE expression: implications for adipocyte triglyceride metabolism. *Am J Physiol Endocrinol Metab* 299:E615–E623.
 73. Hirata M, Yasukawa T, Wiedemann P, et al (2009) Fundus autofluorescence

- and fate of glycoxidized particles injected into subretinal space in rabbit age-related macular degeneration model. *Graefe's Arch Clin Exp Ophthalmol* 247:929–937.
74. Hsieh K, Lee YK, Londos C, et al (2012) Perilipin family members preferentially sequester to either triacylglycerol-specific or cholesteryl-ester-specific intracellular lipid storage droplets. *J Cell Sci* 125:4067–4076.
 75. Burles K, Irwin CR, Burton R, et al (2014) Initial characterization of vaccinia virus B4 suggests a role in virus spread. *Virology* 456–457:108–120.
 76. Anderson DH, Ozaki S, Nealon M, et al (2001) Local cellular sources of apolipoprotein E in the human retina and retinal pigmented epithelium: implications for the process of drusen formation. *Am J Ophthalmol* 131:767–781.
 77. Ishida BY, Bailey KR, Duncan KG, et al (2004) Regulated expression of apolipoprotein E by human retinal pigment epithelial cells. *J Lipid Res* 45:263–271.
 78. Rudolf M, Seckerdieck K, Grisanti S, Curcio CA (2014) Internal structure consistent with remodelling in very small drusen, revealed by filipin histochemistry for esterified cholesterol. *Br J Ophthalmol* 98:698–702.
 79. Maxfield FR, Wüstner D (2012) Analysis of Cholesterol Trafficking with Fluorescent Probes. *Methods Cell Biol* 108:367–393.
 80. Johnson LV, Forest DL, Banna CD, et al (2011) Cell culture model that mimics drusen formation and triggers complement activation associated with age-related macular degeneration. *Proc Natl Acad Sci* 108:18277–18282.

81. Cougnard-Grégoire A, Delyfer M-N, Korobelnik J-F, et al (2014) Elevated high-density lipoprotein cholesterol and age-related macular degeneration: the Alienor study. *PLoS One* 9:e90973.
82. Peyman GA, Spitznas M, Straatsma BR (1971) Peroxidase Diffusion in the Normal and Photocoagulated Retina. *Invest Ophthalmol Vis Sci* 10:181–189.
83. Gaudana R, Ananthula HK, Parenky A, Mitra AK (2010) Ocular drug delivery. *AAPS J* 12:348–360.
84. Jackson TL, Antcliff RJ, Hillenkamp J, Marshall J (2003) Human retinal molecular weight exclusion limit and estimate of species variation. *Investig Ophthalmol Vis Sci* 44:2141–2146.
85. Kim JH, Kim JH, Kim K-W, et al (2009) Intravenously administered gold nanoparticles pass through the blood-retinal barrier depending on the particle size, and induce no retinal toxicity. *Nanotechnology* 20:505101.
86. Chen C, Cano M, Wang JJ, et al (2014) Role of unfolded protein response dysregulation in oxidative injury of retinal pigment epithelial cells. *Antioxid Redox Signal* 20:2091–2106.
87. Liles MR, Newsome DA, Oliver PD (1991) Antioxidant enzymes in the aging human retinal pigment epithelium. *Arch Ophthalmol (Chicago, Ill 1960)* 109:1285–1288.
88. Javitt NB, Javitt JC (2009) The retinal oxysterol pathway: a unifying hypothesis for the cause of age-related macular degeneration. *Curr Opin Ophthalmol* 20:151–157.
89. Owens SL, Bunce C, Brannon AJ, et al (2006) Prophylactic Laser Treatment

- Hastens Choroidal Neovascularization in Unilateral Age-Related Maculopathy: Final Results of the Drusen Laser Study. *Am J Ophthalmol* 141:276–281.
90. Tirlapur UK, König K (2002) Femtosecond near-infrared laser pulses as a versatile non-invasive tool for intra-tissue nanoprocessing in plants without compromising viability. *Plant J* 31:365–374.
 91. König K, Riemann I, Fritzsche W (2001) Nanodissection of human chromosomes with near-infrared femtosecond laser pulses. *Opt Lett* 26:819–821.
 92. Watanabe W, Arakawa N, Matsunaga S, et al (2004) Femtosecond laser disruption of subcellular organelles in a living cell. *Opt Express* 12:4203–4213.
 93. Kohli V, Acker JP, Elezzabi AY (2005) Reversible permeabilization using high-intensity femtosecond laser pulses: applications to biopreservation. *Biotechnol Bioeng* 92:889–899.
 94. Katchinskiy N, Godbout R, Goetz HR, Elezzabi AY (2014) Femtosecond laser-induced cell-cell surgical attachment. *Lasers Surg Med* 46:335–341.
 95. Kollias N, Baqer AH (1987) Absorption Mechanisms of Human Melanin in the Visible, 400–720nm. *J Invest Dermatol* 89:384–388.
 96. Kollias N, Baqer AH (1988) The role of human melanin in providing photoprotection from solar mid-ultraviolet radiation (280-320 nm). *J Soc Cosmet Chem* 39:347–354.
 97. Zonios G, Dimou A, Bassukas I, et al (2008) Melanin absorption

- spectroscopy: new method for noninvasive skin investigation and melanoma detection. *J Biomed Opt* 13:14017.
98. Jacques SL, Glickman RD, Schwartz JA (1996) Internal absorption coefficient and threshold for pulsed laser disruption of melanosomes isolated from retinal pigment epithelium. *Proc Spie* 2681:468–477.
 99. Song W, Zhang L, Ness S, Yi J (2017) Wavelength-dependent optical properties of melanosomes in retinal pigmented epithelium and their changes with melanin bleaching : a numerical study. *Biomed Opt Express* 8:3966–3980.
 100. Jacques SL, McAuliffe DJ (1991) The Melanosome: Threshold Temperature for Explosive Vaporization and Internal Absorption Coefficient During Pulsed Laser Irradiation. *Photochem Photobiol* 53:769–775.
 101. Tanna H, Dubis AM, Ayub N, et al (2010) Retinal imaging using commercial broadband optical coherence tomography. *Br J Ophthalmol* 94:372–376.

Appendix A

Retinal Layer Dimensions

It is important to know the dimensions of the various structures in the retina that a laser treatment beam would encounter during delivery to sub-RPE drusen for ablation. The two most pertinent structures to be aware of during femtosecond ablation of drusen are the RPE and BrM, as they lie just above and below the drusen, respectively. As previously stated in Chapter 1, the RPE cell monolayer averages 10-14 μm thick while the BrM is significantly thinner, typically 2-4 μm in a healthy individual [12, 18]. Optical coherence tomography (OCT) images are a helpful tool in measuring the thickness of the various retinal layers. Figures A.1(a) and A.1(b) show two OCT images of a retina using two different illumination sources. Figures A.1(c) and A.1(d) identify the depth of various retinal boundary layer membranes between the different layers of retinal cells. Comparing the labeled membranes and layers in Fig. A.1(c) and (d) to cross-sections of the retina helps determine the cell layer thicknesses. Figure A.2 is an artificial image of the retinal layers and Fig. A.3 is a histological cross-section of the retina, both with the various structures and layers labeled. Cross-referencing the depth measurements from the OCT images in Fig. A.1 with the retinal sections seen in Fig. A.2 and A.3 indicate the ganglion and bipolar cell layer is 120 μm , the outer nuclear layer is 75 μm , and the photoreceptor layer is 35 μm thick.

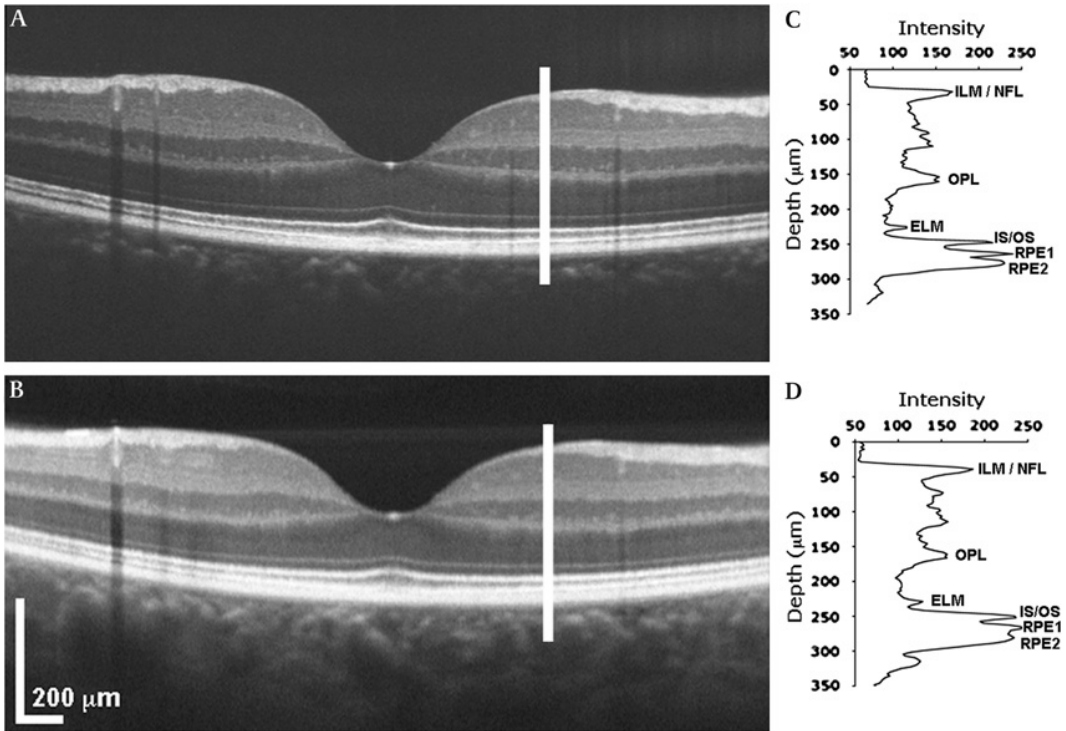


Fig. A.1: OCT image of retina layers. (A) and (B) show two images of the same retina. In (C) and (D) the vertical depths of many identifiable and important retinal membrane layers are plotted along the white lines as seen in (A) and (B). Adapted from [101].

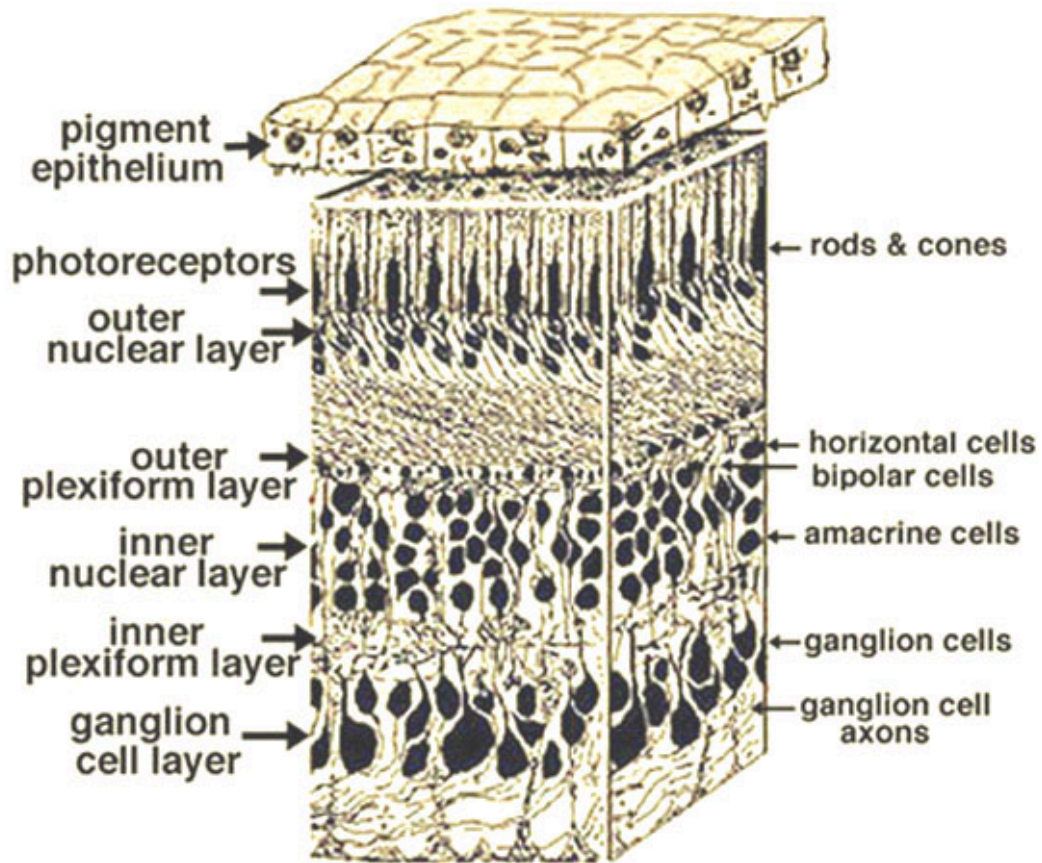


Fig. A.2: Graphical representation of the retina. Many important cell layers and boundary membranes between different cell types are labeled. Adapted from [9].

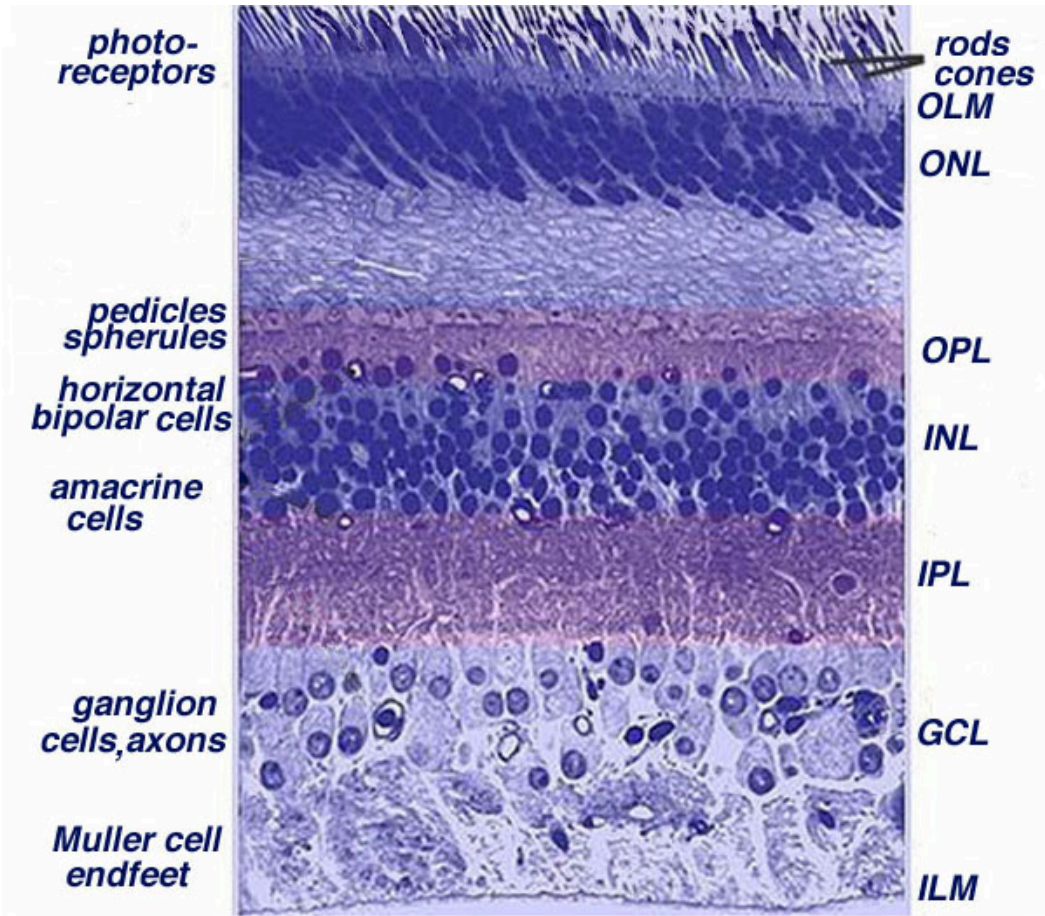


Fig. A.3: Histological cross-section of a human retina. The various cell layers are labeled on the left with the bounding membranes and layers on the right. Outer limiting membrane (OLM). Outer nuclear layer (ONL). Outer plexiform layer (OPL). Inner nuclear layer (INL). Inner plexiform layers (IPL). Ganglion cell layers (GCL). Inner limiting membrane (ILM). Adapted from [9].

Appendix B

Sample Calculations

The depth of focus and the percent absorption by melanin are discussed in Chapter 1 and 4, respectively. Sample calculations for the two values are below.

The depth of focus of the microscope objective lens follows the relation

$$\text{Depth of focus} = \frac{n \lambda}{2 NA^2}$$

where n is the index of refraction of the media, λ is the wavelength of the laser, and NA is the numerical aperture of the objective lens. In our case the media is water with index of refraction of 1.333, the wavelength is 800 nm, and the numerical aperture is 1. This gives a depth of focus of 0.53 μm .

Melanosomes occupy 3.5% of RPE cytoplasmic volume after age 40 [10]. RPE are cuboidal cells and can be approximated to 10 μm in all three dimensions [12]. Therefore, the volume of an RPE cell is $1 \times 10^{-9} \text{ cm}^3$. At 3.5% of cytoplasmic volume the melanosome volume is $3.5 \times 10^{-11} \text{ cm}^3$. Assuming uniform distribution throughout the cell, the thickness of the melanosome layer is therefore $3.5 \times 10^{-5} \text{ cm}$. The transmittance of a material is given by the Beer-Lambert law

$$I = I_0 e^{-\mu_a x}$$

where I is the final intensity, I_0 is the initial intensity, x is the thickness of the layer,

and μ_a is the absorption coefficient of the melanin. Values for melanin absorption coefficient values vary between different sources, at 800 nm absorption coefficient values range between 500 cm^{-1} [98], 300 cm^{-1} [99], and 200 cm^{-1} [100]. For this calculation the absorption coefficient will be taken to be 300 cm^{-1} . Therefore, the ratio of I/I_0 is 0.989, giving a percent transmission of 99%. Therefore, the melanin in the RPE only absorb 1% of incident light from the femtosecond laser.